

# How do galaxies get their gas?

Dušan Kereš,<sup>1</sup>★ Neal Katz,<sup>1</sup>★ David H. Weinberg<sup>2</sup>★ and Romeel Davé<sup>3</sup>★

<sup>1</sup>*Astronomy Department, University of Massachusetts at Amherst, MA 01003, USA*

<sup>2</sup>*Ohio State University, Department of Astronomy, Columbus, OH 43210, USA*

<sup>3</sup>*University of Arizona, Steward Observatory, Tucson, AZ 85721, USA*

Accepted 2005 July 5. Received 2005 June 30; in original form 2004 July 5

## ABSTRACT

We examine the temperature history of gas accreted by forming galaxies in smoothed particle hydrodynamics simulations. About half of the gas follows the track expected in the conventional picture of galaxy formation, shock heating to roughly the virial temperature of the galaxy potential well ( $T \sim 10^6$  K for a Milky Way type galaxy) before cooling, condensing and forming stars. However, the other half radiates its acquired gravitational energy at much lower temperatures, typically  $T < 10^5$  K, and the histogram of maximum gas temperatures is clearly bimodal. The ‘cold mode’ of gas accretion dominates for low-mass galaxies (baryonic mass  $M_{\text{gal}} \lesssim 10^{10.3} M_{\odot}$  or halo mass  $M_{\text{halo}} \lesssim 10^{11.4} M_{\odot}$ ), while the conventional ‘hot mode’ dominates the growth of high-mass systems. Cold accretion is often directed along filaments, allowing galaxies to efficiently draw gas from large distances, while hot accretion is quasi-spherical. The galaxy and halo mass dependence leads to redshift and environment dependence of cold and hot accretion rates, with the cold mode dominating at high redshift and in low-density regions today, and the hot mode dominating in group and cluster environments at low redshift. The simulations reproduce an important feature of the observed relation between the galaxy star formation rate (SFR) and the environment, namely a break in star formation rates at surface densities  $\Sigma \sim 1 h_{75}^2 \text{ Mpc}^{-2}$ , outside the virial radii of large groups and clusters. The cosmic SFR tracks the overall history of gas accretion, and its decline at low redshift follows the combined decline of cold and hot accretion rates. The drop in cold accretion is driven by the decreasing infall rate on to haloes, while for hot accretion this slower mass growth is further modified by the longer cooling times within haloes. If we allowed hot accretion to be suppressed by conduction or active galactic nuclei feedback, then the simulation predictions would change in interesting ways, perhaps resolving conflicts with the colours of ellipticals and the cut-off of the galaxy luminosity function. The transition at  $M_{\text{halo}} \sim 10^{11.4} M_{\odot}$  between cold-mode domination and hot-mode domination is similar to that found by Birnboim & Dekel using one-dimensional simulations and analytic arguments. The corresponding baryonic mass is tantalizingly close to the scale at which Kauffmann et al. find a marked shift in galaxy properties, and we speculate on possible connections between these theoretical and observational transitions.

**Key words:** methods: numerical – cooling flows – galaxies: evolution – galaxies: formation.

## 1 INTRODUCTION

The conventional sketch of galaxy formation has its roots in classic papers of the late 1970s and early 1980s, with initial discussions of collapse and cooling criteria by Rees & Ostriker (1977) and Silk (1977), the addition of dark matter haloes by White & Rees

(1978) and the disc formation model of Fall & Efstathiou (1980). According to this sketch, gas falling into a dark matter potential well is shock heated to approximately the halo virial temperature,  $T_{\text{vir}} = 10^6 (v_{\text{circ}}/167 \text{ km s}^{-1})^2$  K, putting it in quasi-hydrostatic equilibrium with the dark matter. Gas in the dense, inner regions of this shock-heated halo radiates its thermal energy, loses its pressure support, settles into a centrifugally supported disc and forms stars. Mergers of discs can scatter stars on to disordered orbits, producing spheroidal systems, which may regrow discs if they experience subsequent gas accretion. Over the previous decade, the ideas of these seminal papers have been updated and extended into a powerful

★E-mail: keres@nova.astro.umass.edu (DK); nsk@kaka.astro.umass.edu (NK); dhw@astronomy.ohio-state.edu (DHW); rad@astro.as.arizona.edu (RD)

'semi-analytic' framework for galaxy formation calculations (e.g. White & Frenk 1991; Kauffmann, White & Guiderdoni 1993; Cole et al. 1994; Avila-Reese, Firmani & Hernandez 1998; Mo, Mao & White 1998; Somerville & Primack 1999).

The geometry seen in  $N$ -body and hydrodynamic cosmological simulations, where the densest structures often form at the nodes of a filamentary network, is clearly more complicated than the spherical geometry underlying semi-analytic calculations. None the less, a substantial fraction of the gas in these simulations does shock heat to  $T \sim T_{\text{vir}}$ , and some of this gas does cool and settle into galaxies. The approximate agreement between semi-analytic models and smoothed particle hydrodynamics (SPH) calculations of galaxy masses (e.g. Benson et al. 2001; Yoshida et al. 2002; Helly et al. 2003) has therefore been taken as evidence that the conventional sketch, while idealized, captures most of the essential physics. In this paper, we use SPH simulations of cosmological volumes to argue that this sketch requires an important revision: roughly half of the gas accreted by the simulated galaxies is never shock heated close to the halo virial temperature ( $T \sim 10^6$  K for a Milky Way type galaxy) but instead radiates its acquired gravitational energy from  $T \lesssim 2.5 \times 10^5$  K (often  $T \lesssim 5 \times 10^4$  K). This 'cold mode' of gas accretion dominates for lower-mass galaxies (baryon mass  $M_{\text{gal}} \lesssim 2 \times 10^{10} M_{\odot}$ ), while the conventional, 'hot mode' of gas accretion dominates the growth of high-mass systems. As a result, 'cold-mode' accretion dominates at high redshift ( $z \gtrsim 3$ ) and in low-density environments today, while 'hot-mode' accretion dominates in group and cluster environments at low redshift.

There is, in fact, a long history of results suggesting that cold accretion could be an important element of galaxy formation. Binney (1977), using analytic models of protogalaxy collapse, argued that the amount of shock heating could be small for plausible physical conditions, with only a fraction of the gas reaching temperatures  $T \sim T_{\text{vir}}$ . In the first SPH simulations of forming galaxies (Katz & Gunn 1991), which had idealized initial conditions but included small-scale power leading to hierarchical formation, most of the gas never heated above  $T \sim 3 \times 10^4$  K, with much of the cooling radiation therefore emerging in the Ly $\alpha$  line. Katz & White (1993) and Katz et al. (1994) showed the importance of filamentary structures as channels for gas accretion in simulations with cold dark matter (CDM) initial conditions. Recent studies based on SPH simulations of cosmological volumes reveal the situation even more starkly. Fardal et al. (2001) showed that most of the cooling radiation in their simulations comes from gas with  $T < 2 \times 10^4$  K, again implying that a significant fraction emerges in the Ly $\alpha$  line. As gas starting at  $T \sim 10^6$  K must radiate 90 per cent of its thermal energy by the time it cools to  $T \sim 10^5$  K, Fardal et al. (2001) concluded that the majority of the gas entering galaxies (indeed, the majority of the gas experiencing any significant cooling) must not be heated to the virial temperature of any dark matter halo resolved by the simulation. Kay et al. (2000) directly tracked the temperature histories of particles that ended up in their simulated galaxies and found that only 11 per cent of these particles were ever heated to a temperature above  $10^5$  K.

Motivated by these results, here we investigate the temperature histories of accreted gas particles as a function of galaxy mass, redshift and environment, thoroughly quantifying the relative importance of the cold and hot modes of gas accretion in our SPH simulations. We use several simulations to demonstrate the insensitivity of our primary conclusions to numerical resolution over a wide dynamic range. We reported initial results from our study in Katz et al. (2003). Birnboim & Dekel (2003) have investigated similar issues with a complementary approach based on high-resolution,

spherically symmetric collapse calculations. They find that a virial shock fails to develop if the gas cooling time is shorter than the local compression time, so in these cases gas shells fall far inside the halo virial radius without ever being heated to high temperature. Birnboim & Dekel (2003) show that the cooling time condition corresponds approximately to a threshold in the halo mass of the galaxy, with little dependence on redshift. As we will show in Section 3 below, our results are in quite good agreement with Birnboim & Dekel's, despite the radically different approaches. Traditional semi-analytic models also distinguish between haloes with rapid post-shock cooling and haloes with slow post-shock cooling (e.g. White & Frenk 1991), though the distinction has received relatively little attention in discussions of these models, and heating to the virial temperature is assumed in either case. In quantitative terms, we find that cold accretion plays a much larger role in our simulations than rapid-cooling accretion plays in standard semi-analytic calculations (see Section 6.3 and the Appendix).

In addition to being an important aspect of the physics of galaxy formation, the existence of distinct cold and hot modes of gas accretion could have interesting observational implications. Fardal et al. (2001) emphasized one of these implications: cold accretion allows much of the cooling radiation associated with galaxy formation to emerge in the Ly $\alpha$  line instead of the X-ray continuum (see also Haiman, Spaans & Quataert 2000). A reduced role for hot accretion might help to explain why diffuse X-ray emission from late-type galaxy haloes is well below the predictions of standard semi-analytic calculations (Benson et al. 2000). A second class of implications relates to the cosmic star formation history. Murali et al. (2002; hereafter MKHWD) show that galaxies in SPH simulations, such as those analysed here, gain most of their mass through smooth accretion of gas, not through mergers with pre-existing galaxies (at least not galaxies above the resolution limit of the simulation). They further find that the global history of star formation tracks the global history of gas accretion rather than the merger history. In subsequent analysis, we have found that these generalizations hold fairly well on a galaxy-by-galaxy basis (Maller et al., in preparation). Thus, understanding gas accretion is nearly tantamount to understanding the history of star formation, at least in the simulations.

The cosmic star formation history inferred from near-ultraviolet (near-UV) luminosity functions declines sharply between  $z \sim 1$  and 0 (e.g. Madau et al. 1996). While semi-analytic models and hydrodynamic simulations both predict a drop in the global star formation rate (SFR) over this redshift interval, it is difficult to explain the full order-of-magnitude reduction implied by the data (Baugh et al. 2005). Without an ad hoc fix, semi-analytic and numerical calculations also predict continuing gas accretion and star formation in old, massive galaxies, so they have difficulty in reproducing the 'red envelope' of the observed galaxy population as a function of redshift (e.g. Cole et al. 2000). Of course, partitioning the accretion into cold and hot modes does not, in itself, change the simulation predictions, but it may illuminate the physics behind the predicted drop in the SFR and explain differences between numerical and semi-analytic results. The declining SFR is frequently attributed to the longer cooling times in the hotter, lower-density haloes that prevail at low redshift (e.g. Blanton et al. 2000), but the efficiency of cold accretion could be strongly affected by other factors. Furthermore, stellar or active galactic nuclei (AGN) feedback, or heat conduction, could have different effects on the cold and hot accretion modes, as the incoming gas has a different geometry and density. Allowing for such a difference in theoretical models could have interesting observational consequences, as the relative importance of cold and hot accretion depends on redshift, environment and galaxy mass.

The sensitivity of cold and hot accretion rates to environment could also play a role in explaining the well-known morphology–density relation (e.g. Hubble 1936; Dressler 1980; Postman & Geller 1984) and the associated correlation between galaxy SFR and local density (e.g. Lewis et al. 2002; Gomez et al. 2003; Kauffmann et al. 2004). Mergers, ram pressure stripping (Gunn & Gott 1972), galaxy ‘harassment’ by weak perturbations in clusters (Moore et al. 1996; Moore, Lake & Katz 1998), truncation of gas supplies (Larson, Tinsley & Caldwell 1980; Somerville & Primack 1999) and longer cooling times in hotter environments (Blanton et al. 2000) may all contribute to the origin of these correlations. However, environmental effects that shut off cold accretion flows could suppress star formation and disc growth, and they might explain why transitions in galaxy properties appear to start well beyond the virial radii of groups and clusters (Lewis et al. 2002; Gomez et al. 2003). Kauffmann et al. (2003) find a clear transition in galaxy properties at a baryonic mass  $M_b \sim 3 \times 10^{10} M_\odot$ , with lower-mass galaxies having active star formation, low surface mass density and a disc morphology, while higher-mass galaxies have old stellar populations, high surface mass density and a bulge-dominated morphology. The transition that we find between galaxies dominated by cold accretion and galaxies dominated by hot accretion occurs at a similar mass scale and could be connected to this broader transition in galaxy properties.

After briefly describing our simulations and analysis methods in Section 2, we present our basic results on the global significance and mass dependence of cold and hot accretion in Section 3. We assess the numerical robustness of these results in Section 4; in particular, comparing different simulations to show that cold-mode gas accretion is found in simulations with a large dynamic range in mass resolution. We investigate the dependence of the cold and hot accretion rates and the corresponding star formation rates on galaxy environment in Section 5, including a comparison of the predicted correlations between SFR and environment to the Gomez et al. (2003) observations. In Section 6 we describe our current physical understanding of the cold and hot accretion modes and discuss some of the potential implications mentioned above. We summarize our conclusions in Section 7.

## 2 SIMULATIONS AND NUMERICAL METHODS

### 2.1 Simulation parameters

We adopt an inflationary cold dark matter model dominated by a cosmological constant,  $\Lambda$ CDM, with  $\Omega_m = 0.4$ ,  $\Omega_\Lambda = 0.6$ ,  $h \equiv H_0/(100 \text{ km s}^{-1} \text{ Mpc}^{-1}) = 0.65$  and a primordial power spectrum index  $n = 0.93$ . For the amplitude of mass fluctuations we use  $\sigma_8 = 0.8$ , which for our adopted parameters is consistent both with *COBE* normalization using CMBFAST (Seljak & Zaldariaga 1996; Zaldariaga, Seljak & Bertschinger 1998) and with the observed abundance of rich clusters (White, Efstathiou & Frenk 1993). For the baryonic density we adopt  $\Omega_b = 0.02 h^{-2}$ , a value consistent both with the deuterium abundance in high-redshift Lyman-limit systems (Burles & Tytler 1998) and the value derived from cosmic microwave background (CMB) anisotropy measurements (de Bernardis et al. 2002). Our values of  $\Omega_b$ ,  $n$  and  $\sigma_8$  are close to those inferred by recent joint analysis of CMB anisotropy measurements from WMAP (Bennett et al. 2003) and galaxy clustering data from the 2dF Galaxy Redshift Survey (2dFGRS; Colless et al. 2001) and the Sloan Digital Sky Survey (SDSS; York et al. 2000), while our assumed  $\Omega_m$  is higher by  $\sim 1.5\sigma$ . We have recently repeated one of our runs using the parameter values implied by the WMAP analysis

**Table 1.** Parameters of the simulations used in this paper.  $L$  is the comoving box size,  $N$  is the total number of particles (dark+baryonic),  $z_{\text{fin}}$  is the final redshift to which the simulation has been evolved, UV indicates whether or not a UV background is included in the calculation of cooling and heating rates and  $M_{\text{res}}$  is the baryonic mass resolution threshold, corresponding to the mass of 64 gas particles. Our main simulation is marked with bold letters.

Name	$L$ ( $h^{-1}$ Mpc)	$N$	$z_{\text{fin}}$	UV	$M_{\text{res}}(M_\odot)$
L50/144nb	50	$2 \times 144^3$	0	No	$5.4 \times 10^{10}$
<b>L22/128</b>	22.22	$2 \times 128^3$	0	Yes	$6.8 \times 10^9$
L22/64nb	22.22	$2 \times 64^3$	0	No	$5.4 \times 10^{10}$
L11/64	11.11	$2 \times 64^3$	3	Yes	$6.8 \times 10^9$
L11/64nb	11.11	$2 \times 64^3$	3	No	$6.8 \times 10^9$
L11/128	11.11	$2 \times 128^3$	3	Yes	$8.5 \times 10^8$
L5.5/128	5.55	$2 \times 128^3$	3	Yes	$1.1 \times 10^8$

of Spergel et al. (2003), and preliminary investigation shows results similar to those reported here.

Our primary results are derived from a simulation that models a  $22.222 h^{-1}$  Mpc comoving periodic cube using  $128^3$  dark matter particles and  $128^3$  gas particles. Gravitational forces are softened using a cubic spline kernel of comoving radius  $5 h^{-1}$  kpc, approximately equivalent to a Plummer force softening of  $\epsilon_{\text{grav}} = 3.5 h^{-1}$  kpc. Our baryonic mass threshold for resolved galaxies (see Section 2.3) is  $6.8 \times 10^9 M_\odot$ , the mass of 64 gas particles, and there are 1120 galaxies in the box above this threshold at  $z = 0$ . To approximately match our galaxy mass scale to an observed luminosity scale, we note that the Blanton et al. (2003)  $r$ -band luminosity function yields a space density of  $0.0032 h^3 \text{ Mpc}^{-3}$  for galaxies brighter than the characteristic luminosity  $L_*$  of a Schechter (1976) function fit. The baryonic mass threshold that yields the same space density in our simulation is  $2.45 \times 10^{11} M_\odot$ , so if we identify this mass with  $L_*$  and assume that luminosity is approximately proportional to mass, our resolution threshold corresponds roughly to  $L_*/36$ .

We draw on six additional simulations to investigate the influence of mass resolution and the presence of a UV background field on our results. Parameters of all the simulations are listed in Table 1. A simulation of comoving box length  $xh^{-1}$  Mpc and  $N^3$  particles is designated  $Lx/N$ ; thus, our primary simulation is L22/128. Most of the simulations were run with a photoionizing UV background (see below); those that were not are designated ‘nb’ for ‘no background’. The full suite of simulations – L50/144nb, L22/128, L22/64nb, L11/64, L11/64nb, L11/128, L5.5/128 – spans a factor of 512 in mass resolution. However, the highest-resolution simulations (L11/128 and L5.5/128) have been evolved only to  $z = 3$ , and the lowest-resolution simulations have no UV background.

### 2.2 The simulation code

Our simulations are performed using the parallel version of TREESPH (Hernquist & Katz 1989; Katz, Weinberg & Hernquist 1996, hereafter KWH; Davé, Dubinski & Hernquist 1997). This code combines smoothed particle hydrodynamics (Gingold & Mohaghan 1997; Lucy 1977) with the hierarchical tree algorithm for computation of gravitational forces (Barnes & Hut 1986; Hernquist 1987). TREESPH is a completely Lagrangian code, adaptive both in space and in time. In our simulations, gas properties are estimated by smoothing over 32 nearby particles. There are three kinds of particles in our simulations: dark matter, stars and gas. Collisionless particles (dark matter and stars) are influenced only by gravity, while gas particles are influenced by pressure gradients and shocks in addition to gravity.

We use the geometric averaging form of the energy equation (Hernquist & Katz 1989). Gas particles experience adiabatic heating and cooling, shock heating, inverse Compton cooling off the microwave background, and radiative cooling via free–free emission, collisional ionization and recombination, and collisionally excited line cooling. We assume primordial abundances (as we are primarily interested in following gas before it gets into galaxies), and we include only atomic cooling processes, so gas cannot cool below  $T \sim 10^4$  K. In most of our simulations (see above), we include photoionization by a spatially uniform UV background, which heats low-temperature gas and suppresses cooling processes involving neutral atoms at low gas densities. For the spectral shape and intensity of the UV background we use the calculations of Haardt & Madau (1996). Our calculations of cooling and heating rates are discussed in detail by KWH, who also illustrate the influence of photoionization on these rates.

We heuristically include star formation and its associated supernova feedback, as described by KWH. In brief, gas with physical density  $\rho_{\text{gas}} > 0.1 m_{\text{H}} \text{ cm}^{-3}$  (hydrogen number density  $n_{\text{H}} > 0.1 \text{ cm}^{-3}$ ) is assumed to convert into stars on a time-scale set by the dynamical time or the cooling time, whichever is longer. We also require star-forming gas to be Jeans unstable, part of a converging flow ( $\nabla \cdot \mathbf{v} < 0$ ), and above the virial overdensity ( $\rho_{\text{gas}}/\bar{\rho}_{\text{bar}} > 55.7$ ), but gas that satisfies the physical density criterion usually satisfies the other three criteria as well. Gas reaches this high density only after cooling to  $T \sim 10^4$  K, and we implicitly include the subsequent molecular and metal-line cooling to lower temperatures as part of the star formation process. Our formula for the star formation rate leads to a relation with gas surface density similar to a Schmidt law (Schmidt 1959; Kennicutt 1998). At a technical level, we convert gas particles to collisionless star particles by means of intermediate particles that feel reduced gas forces (see KWH). This allows us to trace each star particle back to a unique gas progenitor.

During the formation of stars, supernova feedback energy is added to the surrounding gas particles in the form of heat. This energy is added gradually with an exponential time decay of  $2 \times 10^7$  yr. We calculate this energy assuming that stars with masses above  $8 M_{\odot}$  explode as supernovae, which for our adopted Miller–Scalo initial mass function (Miller & Scalo 1979) gives  $7.35 \times 10^{-3}$  supernovae per solar mass of formed stars. Each supernova deposits  $10^{51}$  erg of energy into the surrounding medium. The surrounding medium is usually dense, so the deposited energy is typically radiated away before it can drive a galactic-scale wind.

### 2.3 Identifying galaxies and haloes

Cosmological simulations that incorporate cooling and star formation produce dense groups of baryonic particles with the sizes and masses of observed galaxies (Katz, Hernquist & Weinberg 1992; Evrard, Summers & Davis 1994). To identify these dense groups we use the group-finding algorithm spline kernel interpolative DENMAX (SKID)<sup>1</sup> (Gelb & Bertschinger 1994; KWH). This algorithm involves four basic steps: (1) determine the smoothed baryonic density field; (2) move baryonic particles towards higher density along the initial gradient of the baryonic density field; (3) define the initial group to be the set of particles that aggregate at a particular density peak; (4) link together initial groups that are very close together; and (5) remove particles from the group that do not satisfy a negative energy binding criterion relative to the centre of mass

of the group. We apply SKID to the population of all star particles and those gas particles that have temperatures  $T < 3 \times 10^4$  K and overdensities  $\rho_{\text{gas}}/\bar{\rho}_{\text{gas}} > 10^3$ , and we henceforth refer to the groups of stars and cold gas that SKID identifies simply as ‘galaxies’. Tests on simulations with varying mass resolution show that the simulated galaxy population becomes substantially incomplete below a baryonic mass corresponding to  $\sim 64 m_{\text{SPH}}$  but is fairly robust above this limit (see, e.g., MKHWD). We therefore adopt  $64 m_{\text{SPH}}$  ( $6.8 \times 10^9 M_{\odot}$  in the L22/128 simulation) as our resolution threshold and ignore lower-mass galaxies in our analysis. Because of our high overdensity threshold for star formation, essentially all star formation in the simulation takes place in galaxies, though some of these are below the resolution limit, and some stars are tidally stripped from galaxies during dynamical interactions.

We identify dark matter haloes using a friends-of-friends (FOF) algorithm (Davis et al. 1985), which selects groups of particles in which every particle has at least one neighbour within a specified linking length. We choose the linking length to correspond to the interparticle separation at one-third of the virial overdensity  $\rho_{\text{vir}}/\bar{\rho}$ , which is calculated for the value of  $\Omega_m$  at each redshift using the fitting formula of Kitayama & Suto (1996). We refine the haloes and assign a virial mass, virial radius and virial temperature using a spherical overdensity (SO) criterion. Specifically, we set the centre of the group to be at the position of the most bound FOF particle, and we go out in radius until the mean enclosed overdensity (dark matter plus baryons) equals  $\rho_{\text{vir}}(z)/\bar{\rho}$ . We define this radius to be  $R_{\text{vir}}$ , the mass within it to be  $M_{\text{vir}}$  and the halo circular velocity to be  $v_{\text{circ}} = (GM_{\text{vir}}/R_{\text{vir}})^{1/2}$ . We define the halo virial temperature by  $kT_{\text{vir}} = (1/2) \mu m_{\text{p}} v_{\text{circ}}^2$ , so it represents the temperature at which the gas would be in hydrostatic equilibrium if the potential well were isothermal. As gas at this temperature would be fully ionized, we adopt  $\mu = 0.59$ , appropriate to fully ionized, primordial composition gas. We associate galaxies with these, refined, SO haloes.

Our minimum galaxy mass  $M_{\text{gal,min}} = 64 m_{\text{SPH}}$  corresponds to a minimum host halo mass  $M_{\text{halo,min}} \approx (\Omega_m/\Omega_b) M_{\text{gal,min}}$ , as the fraction of cold gas in a halo never exceeds the universal baryon fraction by a large factor (though it can sometimes be slightly larger). The corresponding minimum virial temperature is  $T_{\text{vir,min}}(z) \approx 80\,000 (1+z)$  K for the L22/128 simulation, where the  $(1+z)$  factor arises from the increasing physical density at higher  $z$  for fixed virial overdensity. Including the redshift dependence of the virial overdensity makes the pre-factor slightly lower at high redshifts ( $\sim 75\,000$  K) and slightly higher at low redshifts (88 000 K at  $z = 0$ ). Any resolved galaxy in the simulation resides in a dark matter halo with  $T_{\text{vir}} \geq T_{\text{vir,min}}(z)$ .

### 2.4 Determining gas accretion histories

At each of our output redshifts (listed below), we use SKID to identify all galaxies above our  $64 m_{\text{SPH}}$  baryonic mass resolution threshold ( $6.8 \times 10^9 M_{\odot}$  for L22/128). We discard from consideration any galaxy where the progenitor was not resolved at the previous output redshift, as we do not want to count simply passing across the resolution threshold as ‘accretion’. For the remaining galaxies, resolved in both outputs, we identify any gas particles that are in the galaxy at the later redshift but were not in any resolved galaxy at the earlier redshift as smoothly accreted gas. For each of these accreted gas particles, we trace back the entire temperature history since the beginning of the simulation and record the maximum temperature  $T_{\text{max}}$  of the particle. These  $T_{\text{max}}$  values will be used to distinguish the cold and hot accretion modes.

<sup>1</sup> <http://www-hpcc.astro.washington.edu/tools/skid.html>

To determine the global accretion properties at a given redshift, we sum over all the particles that have been smoothly accreted between our previous analysis output and that redshift. By ‘smoothly accreted’ we simply mean particles that were not in resolved galaxies at the previous output. For most of our calculations, we include only accreted *gas* particles in the statistics. Star particles can also be smoothly accreted either because they were in under-resolved galaxies at the previous output or because they were tidally stripped ‘field’ stars. (Often these ‘field’ stars are effectively part of the galactic halo or the intragroup or intracluster environment, but SKID still attaches them to a galaxy.) However, as all the stars in our simulation form within galaxies, the gas that formed these smoothly accreted stars was itself accreted on to a (perhaps under-resolved) galaxy at a higher redshift, making the  $T_{\max}$  values representative of gas accretion at higher redshifts. Including accreted star particles in our statistics has only a small impact, increasing the apparent importance of cold accretion at low redshift (see the dotted line in Fig. 2 below).

Our measured rates of smooth accretion really represent the sum of genuinely smooth gas flow and mergers with galaxies below our resolution limit, including systems that are not even under-resolved bound objects in the simulation but would nevertheless exist in the real Universe. In Section 4.1 we extrapolate the measured distribution of merger mass ratios to show that this subresolution merging is unlikely to be an important correction, so that our measured smooth accretion rates indeed correspond mainly to smooth gas flows.

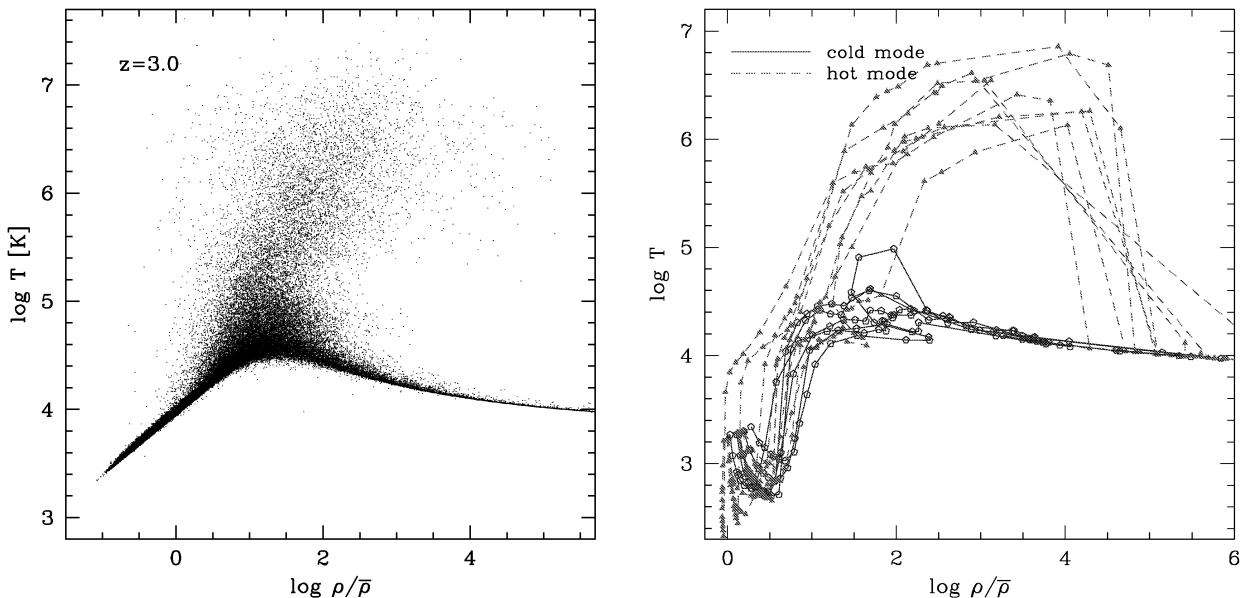
We use the following redshift spacing for determining  $T_{\max}$  values and calculating accretion rates: for  $0 \leq z \leq 1$  we use  $\Delta z \sim 0.125$ , for  $1 < z \leq 3.5$  we use  $\Delta z \sim 0.25$ , for  $3.5 < z \leq 5$  we use  $\Delta z \sim 0.5$ , and for higher redshifts we use  $\Delta z \sim 1$ . In the cosmology we consider here, these redshift intervals correspond to time intervals of roughly  $\Delta t = 0.25$  Gyr for  $z > 3.5$ ,  $\Delta t \sim 0.5$  Gyr at  $z = 1.5$  and  $\Delta t \sim 1.5$  Gyr at  $z = 0$ . These time intervals are close to the typical infall time-scales at the corresponding outputs, except at

$z = 0$  where they are slightly longer. We have checked the effect of using smaller redshift intervals (see Section 4.2) and find that it makes only a small difference to our statistical results.

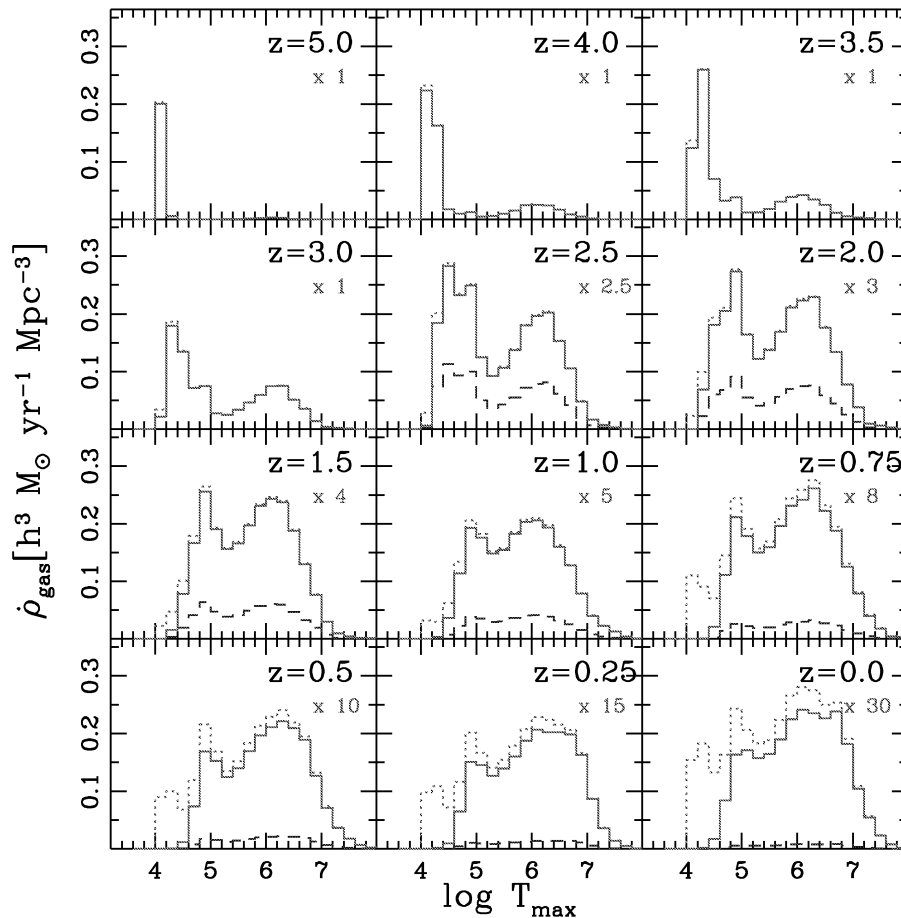
### 3 COLD AND HOT ACCRETION

Fig. 1(a) shows the distribution of gas particles in the temperature–overdensity plane, from the L22/128 simulation at  $z = 3$ . As with previous studies (e.g. Davé et al. 1999), we identify three important gas phases. The narrow, upward-sloping locus with  $\rho/\bar{\rho} < 10$  and  $T < 10^5$  K consists of low-density, highly photoionized gas in the intergalactic medium (IGM), which is responsible for the Ly $\alpha$  forest. The tight temperature–density relation in this regime is maintained by the competition between adiabatic cooling and photoionization heating (Hui & Gnedin 1997). The plume of particles with  $\rho/\bar{\rho} \sim 10$ – $10^4$  and  $T \sim 10^5$ – $10^7$  K is comprised of shock-heated gas in virialized haloes and, at the lower-density end, around filaments. The narrow, downward-sloping locus at  $\rho/\bar{\rho} > 10^3$  and  $T \approx 10^4$  K represents radiatively cooled, dense gas in galaxies. Cooling times at these densities are short, so gas remains close to the equilibrium temperature where photoionization heating balances radiative cooling, which is a slowly decreasing function of density.

According to the conventional sketch described in the introduction, gas that ends up in galaxies starts in the diffuse phase, enters the shock-heated phase, then cools and condenses to reach the galactic phase. Fig. 1(b) plots the  $\rho$ – $T$  trajectories of 15 randomly selected gas particles accreted on to galaxies near  $z = 3$ , starting near  $z = 15$ . Some of these particles follow just the path described above. However, approximately half of them start in the diffuse IGM phase and move directly to the dense galactic phase without ever heating above  $10^5$  K. The virial temperature of the smallest resolved halo in the simulation is  $3.0 \times 10^5$  K at  $z = 3$ , so these particles have never been close to the virial temperature of any resolved halo. The separation between outputs in Fig. 1(b) is typically 0.05–0.1 Gyr, and



**Figure 1.** Left: distribution of gas particles in the  $\rho$ – $T$  plane at  $z = 3$ , in the L22/128 simulation. One can easily identify three major phases: low-density, low-temperature gas in the photoionized IGM, shock-heated overdense gas and high-density radiatively cooled gas within galaxies. Right: trajectories of 15 particles that accreted on to galaxies shortly before  $z = 3$ , illustrating the ‘cold’ (solid lines, circles) and ‘hot’ (dashed lines, triangles) accretion modes. Hot-mode particles are shock heated above  $\sim 10^{5.5}$  K before cooling, while cold-mode particles move directly from the diffuse IGM phase to the dense, galactic phase without ever heating above  $10^5$  K. Trajectories start at  $z = 14.9$  and end at  $z = 3$ . Points mark the individual redshift outputs, which have typical time separations of 0.05–0.1 Gyr.



**Figure 2.** Distribution of maximum temperatures of gas accreting on to galaxies. For each particle that was smoothly accreted on to a resolved galaxy between the previous output and the plotted redshift, we trace back its history to determine the maximum temperature it had at any previous time. Dashed histograms show this distribution in units of  $h^3 M_{\odot} \text{ yr}^{-1} \text{ Mpc}^{-3}$  (comoving) per 0.2-dex bin of  $\log T_{\text{max}}$ . Solid histograms have the same shape but are multiplied by an arbitrary constant (as indicated in the panel) to improve visibility. Dotted histograms show the effect of including accreted stars in the calculation.

some of the low- $T_{\text{max}}$  particles could shock heat and cool rapidly in between two outputs. However, the cooling radiation arguments of Fardal et al. (2001) show that such ‘missed cooling’ events cannot have a large impact. The total energy radiated by gas entering the simulated galaxies is of the order of the acquired gravitational potential energy, as expected, and most of this energy is radiated by gas with  $T < 3 \times 10^4$  K. Gas shock heated to  $10^6$  K, in contrast, would radiate 90 per cent of its thermal energy by the time it cools to  $10^5$  K, so it would not have much energy left to radiate at low temperature. Counting luminosity as Fardal et al. (2001) do closes the loophole of missing rapidly cooling particles because the high luminosity of such particles would compensate for their rarity.

The two populations of trajectories in Fig. 1(b) (also illustrated in fig. 4 of Kay et al. 2000) represent the processes we refer to as ‘cold-mode’ and ‘hot-mode’ gas accretion. To quantify the global significance of these two modes, we plot in Fig. 2 the distribution of  $T_{\text{max}}$  values of accreted gas, computed as described in Section 2.4. Each panel shows the  $T_{\text{max}}$  histogram for particles accreted on to resolved galaxies between the previous output and the indicated redshift. At high redshifts, the histograms are clearly bimodal: some gas enters galaxies after cooling from  $T \sim 10^6$  to  $10^7$  K, but a large fraction of the accreted gas was never hotter than  $T \sim 10^5$  K. The bimodal nature of the  $T_{\text{max}}$  histogram and the compa-

table contributions of the two modes to mass accretion by galaxies are the primary result of this paper.

The overall accretion rate declines towards low redshift, though a significant amount of growth still occurs because more time is available (see Fig. 4 below). The ‘cold-mode’ region of the histogram broadens towards low redshift, and its centroid shifts towards higher  $T_{\text{max}}$ , so by  $z = 0$  the distribution is no longer strongly bimodal. As discussed in Section 2.4, we generally exclude accreted stars from our statistics, as they reflect physical conditions that prevailed at earlier times. Dotted histograms in Fig. 2 show the effect of including accreted stars, which is mainly to extend the low-redshift histograms to lower  $T_{\text{max}}$  values.

Fig. 3 is similar to Fig. 2, but here we plot the distribution of  $T_{\text{max}}/T_{\text{vir}}$ , where  $T_{\text{vir}}$  is the virial temperature of the parent dark matter halo of the galaxy, identified as described in Section 2.3. At  $z \geq 2.5$ , there is again clear bimodality in the distribution, revealing a distinction between gas that goes through a strong, virial-type shock before cooling and gas that does not. The high-temperature portion of the histogram peaks at  $T_{\text{max}} \sim T_{\text{vir}}$  at all redshifts. However, the spread in  $T_{\text{max}}/T_{\text{vir}}$  values is large, roughly an order of magnitude, even for this hot-mode accretion. The spread presumably reflects departures from the spherical geometry adopted in most analytic calculations, plus the effects of post-shock adiabatic compression, which can heat gas to  $T_{\text{max}} > T_{\text{vir}}$  before cooling sets in.

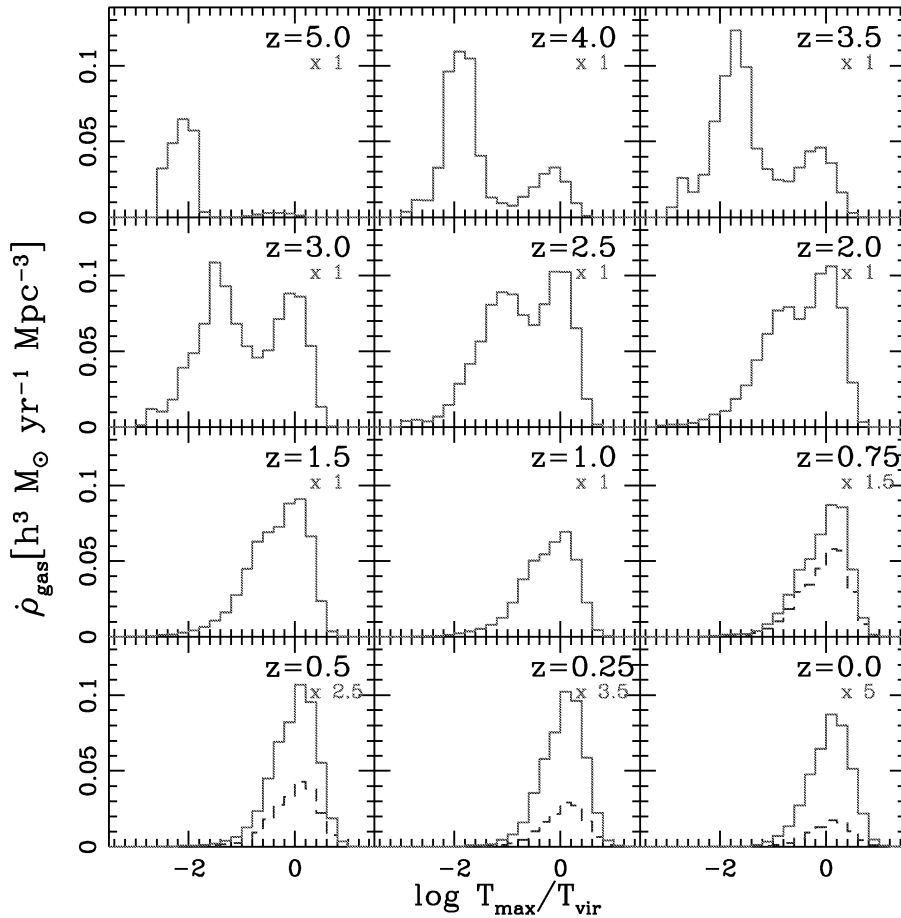


**Figure 3.** Like Fig. 2, but showing the distribution of  $T_{\max}/T_{\text{vir}}$ , the ratio of the maximum temperature of a particle to the virial temperature of the dark matter halo of the accreting galaxy.

The peak of the low-temperature portion of the histogram moves steadily towards higher  $T_{\max}/T_{\text{vir}}$  with time. In Fig. 2 we saw that the characteristic  $T_{\max}$  of cold-mode accretion also increases with time, rising from  $T_{\max} \sim 10^{4.2}$  K at high redshift to  $T_{\max} \sim 10^5$  K at low redshift, but the shift is more rapid when we scale to  $T_{\text{vir}}$  because the virial temperatures of the smallest resolved haloes are themselves dropping with time (see Section 2.3), and these haloes account for a substantial fraction of cold accretion. The clear bimodality of the histograms has therefore disappeared by  $z \sim 1.5$  in Fig. 3, and at lower redshift the cold mode appears as a tail of the distribution towards low  $T_{\max}/T_{\text{vir}}$ .

Figs 2 and 3 show that the cold and hot modes separate more cleanly in the distribution of physical temperature  $T_{\max}$  rather than the scaled temperature  $T_{\max}/T_{\text{vir}}$ . This result is itself a useful clue to the physics of cold accretion. If the characteristic temperature of the cold accretion mode were determined by gravitationally induced shocks, then we would expect it to scale with the characteristic dynamical temperature  $T_{\text{vir}}$ . In this case, the minimum in the  $T_{\max}/T_{\text{vir}}$  histogram should stay roughly constant, instead of rising steadily with time as it does in Fig. 3. The minimum of the  $T_{\max}$  histogram, on the other hand, does stay nearly constant at  $T_{\max} \sim 10^{5.4}$  K, near a local minimum in the atomic cooling curve where free–free emission takes over from helium line cooling (see, e.g., fig. 1 of KWH). This behaviour could arise if a significant fraction of infalling gas starts at low temperature ( $T \lesssim 10^4$  K) and gains energy through

weak shocks or adiabatic compression, in which case gas with short cooling times could radiate energy without ever heating to high temperature, while gas with long cooling times could not. Clearly, this is not the full story, as the peak of the  $T_{\max}$  histogram does move to higher temperature over time, presumably reflecting the higher infall velocities associated with larger gravitationally induced structures. We will discuss the physics of cold accretion at greater length in Section 6.2. For now, we use the empirical evidence of Fig. 2 to set the dividing line between the cold and hot modes at  $T_{\max} = 2.5 \times 10^5$  K, noting that the location of this division is likely to be a consequence of atomic physics. Gravitationally scaled temperatures appear less effective at distinguishing hot and cold accretion.

Fig. 2 shows that cold accretion dominates over hot accretion at high redshift, and then becomes steadily less important at lower redshifts. Fig. 4 quantifies this dependence by showing the mean accretion rate in cold and hot modes as a function of time and redshift. The left-hand panel adopts our standard division between cold and hot mode, at  $T_{\max} = 2.5 \times 10^5$  K. The cold accretion rate and the total accretion rate rise rapidly together and peak at  $z \sim 3$ , and then decline towards low redshift. Note that this figure shows accretion on to galaxies above our resolution threshold; if we went further down the mass function, the accretion rate would be flatter at  $z > 3$ . The hot accretion rate rises later, peaking at  $z \sim 2$ , and it declines more gently thereafter. Cold accretion dominates at  $z \geq 3$ , while hot accretion dominates at  $z \leq 2$ . The right-hand panel

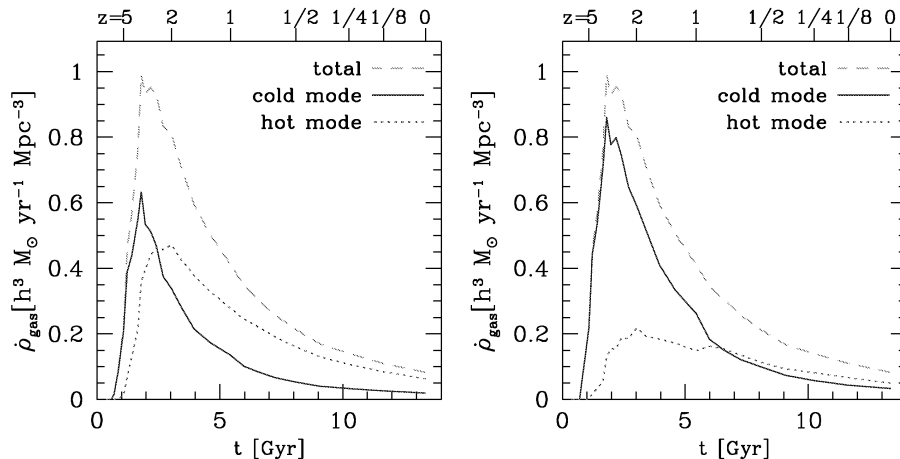


**Figure 4.** Redshift history of the total smooth gas accretion rate (dashed line), and the rates in cold mode and hot mode (solid and dotted lines, respectively). In the left-hand panel, the division between hot and cold modes is at  $T_{\max} = 2.5 \times 10^5$  K, while in the right-hand panel it is at  $T_{\max}/T_{\text{vir}} = 1$ .

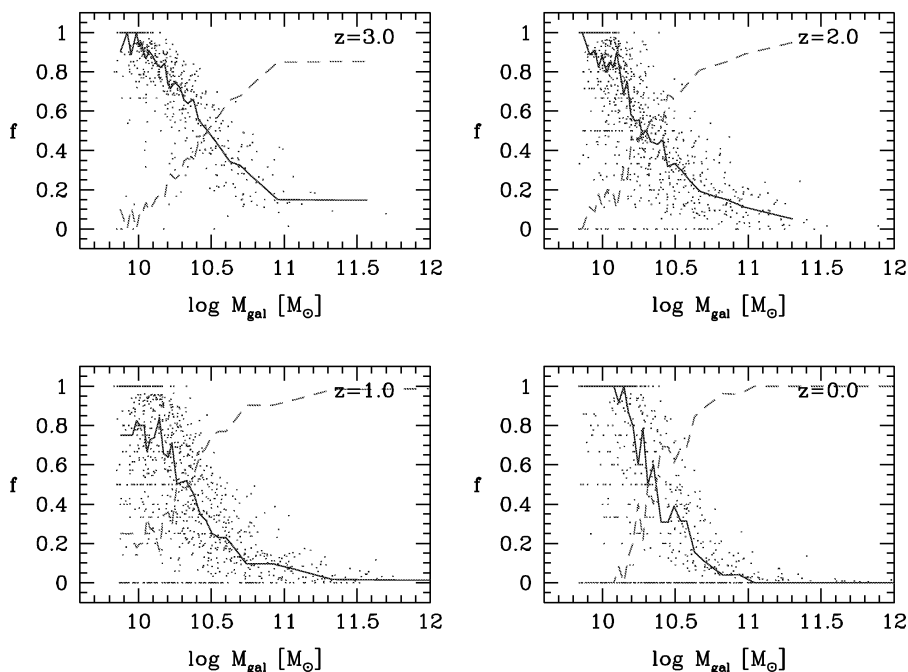


**Figure 5.** The cold accretion fraction as a function of galaxy baryonic mass (cold gas + stars), at  $z = 3, 2, 1$  and  $0$ . Points show the cold fractions of individual galaxies, and solid lines show the median values in bins of baryonic mass. Dashed lines show the median hot fraction; solid and dashed curves sum to one by definition.

adopts a division at  $T_{\max}/T_{\text{vir}} = 1$ . With this definition (which is not, we think, the most appropriate one), cold accretion dominates by a large factor at high redshift, and the two modes are comparably important at  $z < 1$ .

These global statistics, averaged over the full resolved galaxy population, mask an important underlying trend, namely a strong dependence of the cold–hot accretion fractions on galaxy mass. Fig. 5 plots the cold accretion fraction against galaxy baryonic mass at  $z = 3, 2, 1$  and  $0$ . Points show the cold fractions for each resolved galaxy, the solid curve shows the median value in bins with an equal number of galaxies (usually  $\sim 10$ – $20$   $\text{bin}^{-1}$ ), and the dashed curve shows the median hot accretion fraction. The solid and dashed curves sum to one by definition. There is a strong and continuous trend of cold accretion fraction with baryonic mass. The transition

mass where cold and hot accretion are equally important is nearly constant at  $M_{\text{gal}} \sim 10^{10.3} M_{\odot}$  for  $z \leq 2$ , and slightly higher ( $M_{\text{gal}} \sim 10^{10.5} M_{\odot}$ ) at  $z = 3$ . We will show in Section 4.3 that the value of this transition mass is insensitive to the numerical resolution of the simulation. The overall change of the cold-mode accretion fraction with redshift, seen in Fig. 4, is largely a consequence of increasing galaxy masses at low redshift.

We obtain similar results if we use, in place of the baryonic mass of a galaxy, the total mass of its parent halo, as shown in Fig. 6. At high redshift, the trend with halo mass is even cleaner than the trend with galaxy mass; comparing Figs 5 and 6 shows that the low-mass galaxies that are dominated by the hot mode are mostly those that live in high-mass haloes (satellite objects orbiting a larger central galaxy). The cold-mode fraction in massive haloes is slightly



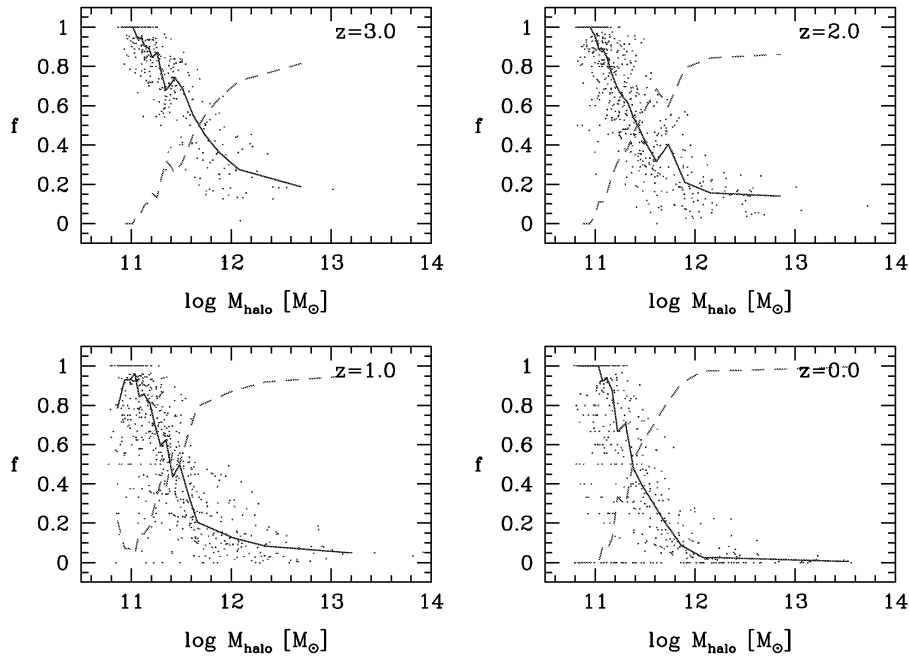


**Figure 6.** Like Fig. 5, but using the parent halo mass in place of the galaxy baryonic mass.

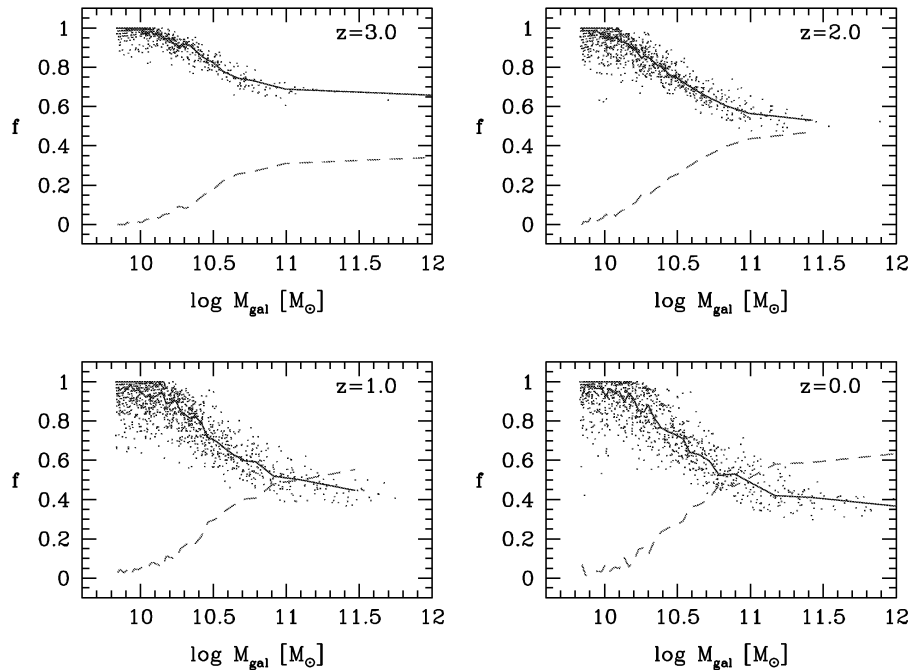


**Figure 7.** Contribution of cold and hot accretion to total galaxy masses at  $z = 3, 2, 1$  and  $0$ . Points show the cold-mode fraction of each galaxy, i.e. the fraction of its mass with  $T_{\max} < 2.5 \times 10^5$  K, as a function of the baryonic mass. The solid line is the median cold-mode fraction, while the dashed line is the median hot-mode fraction; by definition, the two fractions sum to one.

larger at high redshifts, an effect that is even more pronounced if we associate galaxies with FOF haloes instead of SO haloes. The transition halo mass at which cold and hot modes are equally important is  $M_{\text{halo}} \sim 10^{11.4} M_{\odot}$  (slightly higher at  $z = 3$ ), which is the value one would expect given our transition baryonic mass of  $M_{\text{gal}} \sim 10^{10.3} M_{\odot}$  if approximately two-thirds of the available halo baryons typically end up in the central galaxy. The  $10^{11.4} M_{\odot}$  tran-

sition mass is approximately a factor of 2–3 higher than the value found by Birnboim & Dekel (2003) based on one-dimensional (1D) numerical experiments, a good level of agreement given the radically different calculational methods. We will return to this point in Section 6.2.

Fig. 7 characterizes the overall contributions of cold accretion to the simulated galaxy population by plotting the fraction of the

baryonic mass of each galaxy that was first accreted in the cold mode against the present mass of the galaxy. Here we consider all particles present in the galaxy, cold gas *and* stars, and trace back the history of each particle to determine its  $T_{\max}$  value. (As each star particle comes from a unique gas particle, this value is well defined even for stars.) High-mass galaxies have little or no cold gas accretion (Fig. 5), but they are built largely from mergers of lower-mass systems, and these did accrete a significant fraction of their gas in the cold mode. Thus, even for the most massive galaxies present at  $z = 0$  (lower right-hand panel), roughly 40 per cent of the baryonic mass was never heated above our adopted threshold of  $2.5 \times 10^5$  K. For galaxies with  $M_{\text{gal}} < 5 \times 10^{10} M_{\odot}$ , more than half of the mass was accreted in the cold mode, and for  $M_{\text{gal}} \lesssim 2 \times 10^{10} M_{\odot}$ , nearly all of it. If we look at higher redshifts, the cold-mode fraction at fixed mass is slightly higher, but the biggest difference is that more of the galaxies are low mass. Every galaxy present in the simulation at  $z = 3$  was built primarily via cold accretion. We conclude that, if our simulation predictions are accurate, cold accretion is a major ingredient in the recipe of galaxy formation.

## 4 NUMERICAL ISSUES

### 4.1 Subresolution merging

One issue of both physical and numerical interest is whether the ‘smooth’ accretion on to our resolved galaxies has a substantial contribution from mergers with systems below our resolution threshold, as we do not distinguish between gas particles that enter individually and those that enter in unresolved groups (see Section 2.4). If subresolution merging dominates, then our computed  $T_{\max}$  values could be spuriously low because the gas does its cooling in unresolved systems, and the cold accretion process found here might simply be analogous to the mergers with low- $T_{\text{vir}}$  objects. The best way to address this issue is to run a simulation that resolves galaxies all the way down to the limit where their formation is suppressed by the UV background, a baryonic mass of  $\sim M_{\text{gal}} = 10^8 M_{\odot}$  (Efstathiou 1992; Quinn, Katz & Efstathiou 1996; Thoul & Weinberg 1996; Gnedin 2000). We have one such simulation, L5.5/128 with 64 times the mass resolution of L22/128, which has been evolved to  $z = 3$ . We first calculate the smooth accretion rates in L5.5/128 for galaxies above the L22/128 resolution limit, counting as smooth accretion all the gas in galaxies below this limit just as we do in our analysis of L22/128 itself. We then calculate the fraction of this inferred smooth accretion that is actually due to mergers with galaxies between the  $1.1 \times 10^8 M_{\odot}$  resolution threshold of L5.5/128 and the  $6.8 \times 10^9 M_{\odot}$  threshold of L22/128. We find that this fraction is less than 7 per cent at  $z = 3$  and less than 3 per cent at  $z = 4$ . Our treatment of photoionization in these simulations assumes ionization equilibrium (KWH). If we included non-equilibrium heating at the epoch of reionization (Miralda-Escudé & Rees 1994), then our IGM temperature would be somewhat higher, and galaxy formation would be physically suppressed at a higher mass scale (Gnedin 2000), further reducing the subresolution merger contribution.

At  $z < 3$  we do not have such a high-resolution simulation available, so we must use an indirect method to estimate subresolution merging. Our approach is similar to that of MKHWD, based on extrapolating the mass distribution of resolved galaxies that merge with larger resolved galaxies. This distribution is plotted in Fig. 8, for the L22/128 simulation. We consider all resolved mergers that take place in four redshift intervals:  $z \leq 0.5$ ,  $0.5 < z \leq 1$ ,  $1 < z \leq 2$  and  $2 < z \leq 3$ . We fit a power law  $dP_M/d\log M \propto M^{\alpha}$  to the low-mass bins in each panel, where  $dP_M/d\log M$  is the probability per d

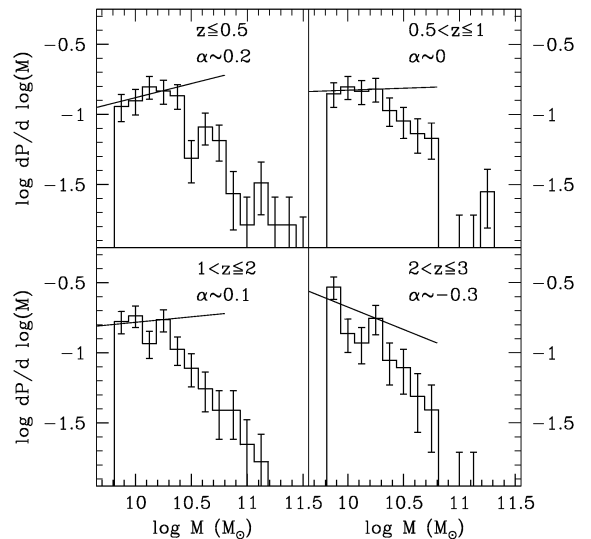


**Figure 8.** The mass spectrum of galaxies that merge with larger galaxies, in four redshift intervals as indicated. We fit power laws to the low ends of these distributions as described in the text. Straight lines show these fits, which have logarithmic slopes  $\alpha$  as listed.

$\log M$  for a galaxy of mass  $M$  to merge with a larger galaxy. We use the last five bins for the  $z \leq 0.5$  distribution and the last four bins for the other distributions. We force the fits to go through the measured value in the fourth bin, so that we have just one free parameter,  $\alpha$ . Best-fitting slopes range from 0.2 ( $z \leq 0.5$ ) to  $-0.3$  ( $2 < z \leq 3$ ), though the small number of bins and substantial Poisson error bars make these estimates uncertain. The mass contributed per d  $\log M$  scales as  $M^{\alpha+1}$ , so high-mass satellites dominate merger growth if  $\alpha > -1$ , as we find at all redshifts.

Integrating our power-law fits from the resolution limit  $M_{\text{gal}} = 6.8 \times 10^9 M_{\odot}$  down to  $M_{\text{gal}} = 10^8 M_{\odot}$  yields an upper limit to the amount of subresolution merging, as the merger mass distributions appear to be turning over steadily and are likely to fall below our extrapolations. With this estimate, the ratio of mass added to the galaxy population by subresolution mergers to mass added by resolved mergers is approximately 0.1–0.15 at  $z = 0$ –0.5, 0.20–0.35 at  $z = 0.5$ –1, 0.25–0.45 at  $z = 1$ –2, and 0.5–2.0 at  $z = 2$ –3. The quoted ranges reflect the  $1\sigma$  statistical uncertainties in the fitted slopes. Subresolution merging could thus make a significant contribution to merger rates at higher redshifts, but because merger rates are much lower than smooth accretion rates (see Fig. 12 below), it still does not substantially change the inferred accretion rates. The exception is at  $z = 2$ –3, where the maximal correction above could raise the merger rate from 25 per cent of the smooth accretion rate to 150 per cent of the smooth accretion rate. In other words, up to half of our estimated smooth accretion rate at  $z = 2$ –3 could be due to subresolution merging. However, at  $z = 3$  we have direct evidence from the comparison of the L5.5/128 and L22/128 simulations that the unresolved merger rate is only  $\sim 7$  per cent of the smooth accretion rate, implying that our power-law extrapolation greatly overestimates the subresolution merging at high redshift, where the typical galaxy mass is only a few times the resolution limit. We hope to eventually redo our analysis with higher-resolution simulations that model larger volumes than L5.5/128 and continue all the way to  $z = 0$ , but for now we conclude that the quantity we estimate as the smooth accretion rate in the L22/128 simulation does represent truly smooth gas accretion, with only a modest

contribution from subresolution mergers. We thus confirm the conclusion of MKHWD concerning the mechanisms of galaxy growth: typical galaxies gain most of their mass through smooth accretion of gas rather than mergers with smaller galaxies.<sup>2</sup> Furthermore, the cold accretion process that is the focus of this paper is not a consequence of galaxies accreting gas that has cooled in haloes of low virial temperature.

## 4.2 Time resolution

A second technical issue is the time interval between our analysis outputs. As  $T_{\max}$  is by definition the maximum temperature of a particle during its pre-accretion history, our analysis at discrete outputs necessarily yields a lower limit to the true  $T_{\max}$  value of any particle. The arguments of Fardal et al. (2001) imply that we cannot be drastically underestimating  $T_{\max}$  by missing rapidly cooling particles, as these would then have high luminosities that would cause the cooling radiation to emerge mainly at high temperatures, which it does not. However, we have also carried out a direct check by repeating our analysis at several  $z \geq 1$  outputs using our standard time interval to determine which particles are smoothly accreted but determining  $T_{\max}$  values at smaller intervals (by a factor of  $\sim 4$  at  $z = 3$ ,  $\sim 8$  at  $z \sim 2$  and  $\sim 20$  at  $z = 1$ ). With this reanalysis, we find that 15–25 per cent of the smoothly accreted gas that was previously attributed to cold-mode accretion is actually hot-mode accretion, with the larger fraction applying at low redshift when the cold fraction is itself small. Further investigation shows that most of the ‘missed’ hot particles shock heat well inside the virial radius, where the density of the gas is high and the cooling times are short, so they are physically distinct from the ‘classic’ hot-mode particles heated at the virial shock. With higher time resolution, the  $T_{\max}$  distribution of hot-mode particles also shifts towards slightly higher temperatures. Note, however, that if we use higher time resolution for all aspects of our analysis, rather than just for computing  $T_{\max}$  values, then we can actually obtain an increase in the cold-mode fraction at higher redshift, as the calculation now incorporates low-mass galaxies that were previously omitted because they were below the resolution limit at the preceding redshift output. Using the finer time resolution described above to identify galaxies and compute  $T_{\max}$  values yields a net increase in the cold-mode fraction of 30 per cent at  $z \sim 1$ , no significant change at  $z \sim 3$  and a small drop at higher redshifts.

We conclude that the finite time resolution in our analysis may cause errors of  $\sim 0.1$ – $0.2$  in our estimates of global cold and hot accretion fractions. This weak dependence on time resolution makes sense if we ask how far inside a halo a particle needs to be to become shock heated and cool before the next output redshift, and thus be misidentified as cold accretion. Our regular analysis interval is  $\Delta t \sim 1.0$  Gyr at low redshifts and  $\Delta t \sim 0.2$  Gyr at high redshifts. Table 2 lists the time required for gas to cool from  $10^6$  or  $2 \times 10^6$  K

<sup>2</sup>This agreement is, however, somewhat fortuitous. MKHWD applied the power-law extrapolation method to the L50/144nb simulation, but their fig. 9 incorrectly labels the merger mass distribution as being per  $dM$  instead of  $d \log M$  (the quantity they actually calculated). This translates to an error in the power-law coefficient, which caused MKHWD to underestimate the subresolution merging. If MKHWD had correctly applied their power-law fit to their data, they would have concluded that subresolution merging exceeds the true smooth accretion rates. The higher resolution of the L22/128 simulation allows us to see a turnover in the merger mass distribution, which is why we find a small subresolution contribution from correct application of the same method.

**Table 2.** Cooling times in Myr of gas at specified overdensity and redshift, for starting temperatures  $T = 10^6$  K (top) and  $T = 2 \times 10^6$  K (bottom).

Redshift	$\rho/\bar{\rho} = 500$	$\rho/\bar{\rho} = 1000$	$\rho/\bar{\rho} = 5000$	$\rho/\bar{\rho} = 10000$
$T = 1 \times 10^6$ K				
$z = 1$	1030	513	103	51
$z = 2$	304	152	30	15
$z = 3$	128	64	12.8	6.4
$z = 4$	65.6	33	6.6	3.3
$T = 2 \times 10^6$ K				
$z = 1$	2350	1175	235	118
$z = 2$	696	348	69.6	34.8
$z = 3$	294	147	29.4	14.7
$z = 4$	150	75.2	15	7.5

(typical halo virial temperatures) down to  $10^5$  K, at various redshifts and overdensities. We compute these times by integrating over the actual cooling function. For our standard time interval, a particle heated to  $2 \times 10^6$  K cannot cool to  $T = 10^5$  K between two redshift outputs unless its overdensity is greater than 500, corresponding to less than one-third of the virial radius for an isothermal halo. For a particle heated to  $T = 10^6$  K, the cooling time at overdensity 500 is comparable to our standard time interval, which means that the cooling time at the virial radius is much longer than the time interval between our simulation outputs. For our finer time interval, a shock-heated particle would only cool between two outputs for an overdensity of several thousand, requiring it to be very close to the cold baryon component of the galaxy.

## 4.3 Numerical convergence

The most serious numerical concern is that our basic result, the existence of a cold accretion mode that makes a major contribution to galaxy formation, is somehow an artefact of the finite mass resolution of the simulations. For example, numerical broadening of shocks might allow gas to radiate energy while it is passing through the shock, instead of first heating and then cooling (Hutchings & Thomas 2000). We can address this issue by comparing simulations with different mass resolution to check the stability of the results.

The top panels of Fig. 9 compare the  $T_{\max}$  distributions of gas accreted at  $z = 3$  and 4 in the L22/128 simulation and the higher-resolution L11/128 simulation. In L11/128, we only consider the accretion on to galaxies above the  $6.8 \times 10^9 M_{\odot}$  resolution limit of L22/128. These objects are resolved by at least 512 gas and star particles in L11/128. Despite the factor of 8 difference in mass resolution, the two histograms agree nearly perfectly at  $z = 4$ , and they show only modest differences at  $z = 3$ . As the simulation volumes are also different, we expect some differences between these simulations just because of the different structures they contain. The lower panels of Fig. 9 compare the L11/128 and L11/64 simulations, which have identical initial conditions (except for the additional high-frequency modes in L11/128) and differ only in mass resolution. The change of simulation volume slightly improves the agreement at  $z = 3$ , but it appears that most of the difference between L22/128 and L11/128 is an effect of resolution rather than simulation volume. Higher resolution lowers the overall gas accretion rate by  $\sim 30$  per cent. Some of the gas accreted in the lower-resolution simulation is converted into stars within galaxies below the resolution limit of the lower-resolution simulation, but that are resolved in the higher-resolution

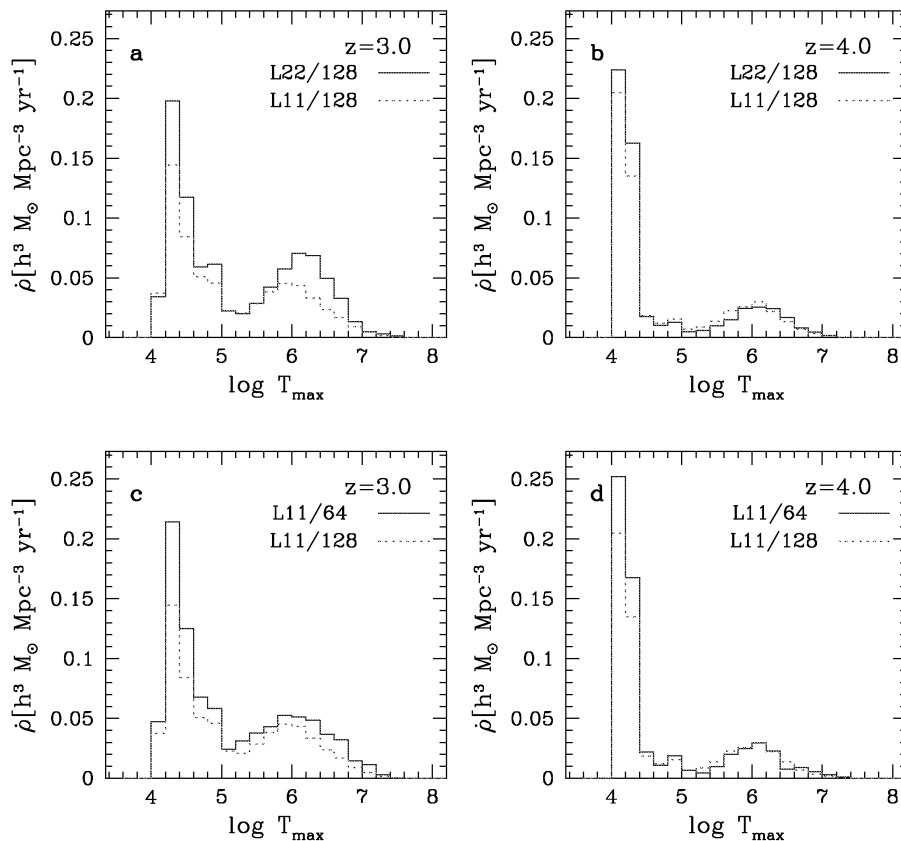


**Figure 9.** Dependence of the  $T_{\max}$  distribution on numerical resolution. Upper panels compare results from our standard, L22/128 simulation (solid histogram) to results from the higher-resolution L11/128 simulation (dotted histogram) at  $z = 3$  (left) and 4 (right). Differences can be partly attributed to resolution and partly to the simulation volume. Lower panels isolate the resolution effect by comparing simulations L11/128 and L11/64, which have the same initial conditions and volume and differ only in mass resolution.

simulation, before it is accreted on to a galaxy above the 512-particle threshold. This can explain a significant part of the differences in the cold-mode accretion rates. However, numerical resolution effects on the gas cooling are probably responsible for most of the differences in the hot-mode accretion rates and the remaining cold-mode differences. These numerical effects must depend on the galactic mass, as at  $z = 4$ , where galaxies are significantly smaller on average, the differences are smaller. As the difference between L22/128 and L11/128 is fairly small and mainly attributable to mass resolution, we conclude that the volume of the L22/128 simulation is large enough to give reasonably accurate statistics on the cold and hot accretion fractions, at least at  $z = 3$ .

Our most powerful test of numerical convergence comes from examining the galaxy mass dependence of the cold accretion fraction, as shown for the L22/128 simulation in Fig. 5. Fig. 10(a) repeats the  $z = 3$  panel of Fig. 5, and Fig. 10(b) shows the same result for the L11/128 simulation. While the higher-resolution simulation contains few high-mass galaxies because of its small volume, the transition between cold- and hot-mode domination occurs at  $M_{\text{gal}} = 10^{10.7} M_{\odot}$ , close to the transition in L22/128. Our highest-resolution simulation, L5.5/128, contains only nine galaxies above the L22/128 mass resolution limit at  $z = 3$  (and only one at  $z = 4$ ), so a comparison of similar form is not very useful. However, we can check the mass dependence of the cold accretion fraction by following the largest (and thus best resolved) galaxy in the simulation volume. Fig. 10(c) plots the cold and hot accretion fractions of this largest galaxy as it grows from  $M_{\text{gal}} = 1.4 \times 10^{10} M_{\odot}$  ( $8000 m_{\text{SPH}}$ ) at  $z = 6$

to  $M_{\text{gal}} = 7.4 \times 10^{10} M_{\odot}$  ( $43\,000 m_{\text{SPH}}$ ) at  $z = 3$ , the redshift of our last simulation output. The transition between hot- and cold-mode dominance occurs close to the  $z = 4$  output, when the galaxy mass is  $M_{\text{gal}} = 10^{10.7} M_{\odot}$ . This agrees well with the transition mass at  $z = 3$  found in L11/128 and L22/128 (and agrees even better with the  $z = 4$  transition mass, which is  $10^{10.75} M_{\odot}$  for L22/128). The second most massive galaxy in L5.5/128 does not reach the cold-hot transition mass until  $z = 3$ , the final output, so it is not useful for this test. The agreement in transition mass over simulations that span a factor of 64 in mass resolution is the strongest single piece of evidence that the importance of cold accretion in our simulations is not an artefact of limited resolution.

#### 4.4 Influence of the UV background

Fig. 11(a) illustrates the impact of the UV background on  $T_{\max}$  distributions, comparing results from L11/64 and L11/64nb at  $z = 3$ . The no-background simulation shows a somewhat reduced hot mode, and the cold accretion is sharply peaked at  $T_{\max} \approx 10^4$  K. The UV background is the only difference between these two simulations. The different amplitude and shape of the histogram at low  $T_{\max}$  is therefore driven by the difference in input physics, most likely the fact that photoionization reduces the strength of the collisional line peak in the cooling curve at moderate overdensity (see KWH, fig. 2). The transition mass at which cold and hot accretion rates are equal is consistently higher in simulations with no UV background, increasing the global contribution of cold accretion.

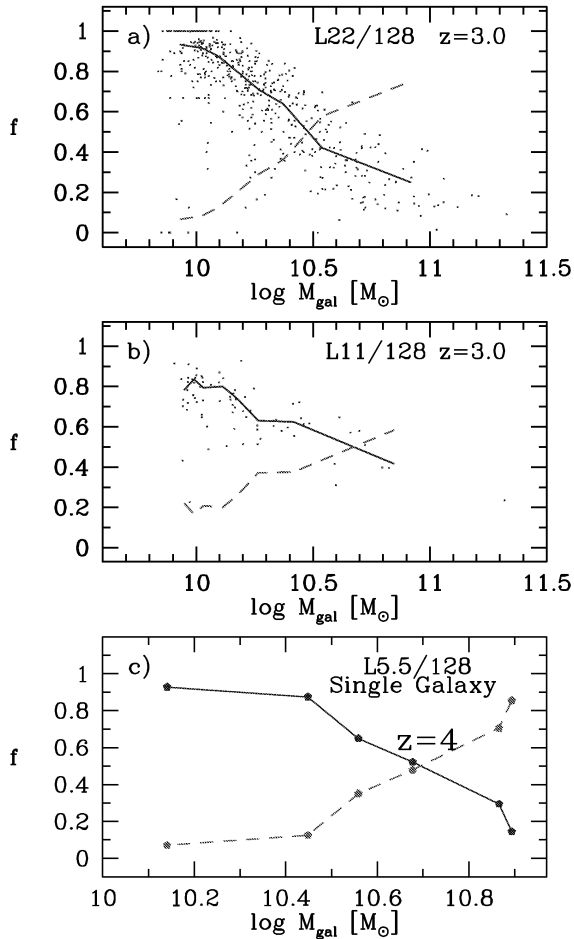


**Figure 10.** Resolution tests of the cold accretion fraction. (a) Cold fraction versus galaxy baryon mass for the L22/128 simulation at  $z = 3$ , repeated from Fig. 5. Points show individual galaxies, the solid line shows the median cold fraction and the dashed line shows the median hot fraction. (b) Same plot for the L11/128 simulation, at  $z = 3$ . (c) Cold fraction versus galaxy baryonic mass for the single largest galaxy in the L5.5/128 simulation at redshifts  $z = 5.5, 5, 4.5, 4, 3.5$  and  $3$  (each point is a redshift, with the highest redshift corresponding to the lowest mass). The dashed line shows the hot fraction. While the mass resolution of this simulation is 64 times higher than that of L22/128, the crossover between cold-mode domination and hot-mode domination occurs at nearly the same baryonic mass.

L22/128 is the highest-resolution simulation we have evolved to  $z = 0$ . All of our lower-resolution simulations have been evolved without a UV background, because photoionization at low-mass resolution spuriously suppresses galaxy formation (Weinberg, Hernquist & Katz 1997). Fig. 11(b) compares the  $z = 0$   $T_{\max}$  histograms from L22/128, L22/64nb and L50/144nb. We now consider only the accretion on to galaxies above the 64-particle threshold of the lower-resolution simulations,  $M_{\text{gal}} = 5.4 \times 10^{10} M_{\odot}$ , which is higher than the cold-hot transition mass of  $\sim 3 \times 10^{10} M_{\odot}$  found for L22/128 at  $z = 0$  (see Fig. 5). As a result of this higher threshold mass, the low-temperature end of the  $T_{\max}$  histogram for L22/128 is strongly suppressed relative to the corresponding histogram in Fig. 2. The no-background simulations, in contrast, show a significant amount of cold accretion, with  $T_{\max}$  values peaked just above  $10^4$  K. Although the simulations differ in both numerical parameters and input physics, the similarity to Fig. 11(a) implies that the UV background is the cause of this difference.

The L22/64nb and L50/144nb simulations also show significantly more hot accretion at  $z = 0$  than L22/128; a similar effect is seen at  $z = 3$  (not plotted). Here we suspect that the coarse resolution of the no-background simulations is to blame, as photoionization has a minimal effect on cooling at high temperatures and the differences are similar to those seen in Figs 9(a) and (c) (at  $z = 3$ ). Finally, we note that the reasonably good agreement between L22/64nb and L50/144nb suggests that the  $22 h^{-1}$  Mpc box is large enough to give representative statistics for the cold-hot fraction even at  $z = 0$ , except perhaps at very large  $T_{\max}$ .

#### 4.5 Other simulations

Within our own set of simulations, we find that the existence of an important cold accretion mode is insensitive to mass resolution or simulation volume, though the specifics of the  $T_{\max}$  distribution are significantly affected by the presence of a UV background. SPH simulations of the formation of individual galaxies achieve still higher resolution, with thousands of particles in the central object, and they also show a large fraction of cold accretion (Katz & Gunn 1991; Abadi et al. 2003). Further evidence of the robustness of the result comes from simulations of volumes such as those considered here performed with entirely independent SPH codes. Kay et al. (2000), studying a  $2 \times 32^3$  particle simulation of a  $10 h^{-1}$  Mpc box performed by the Virgo consortium, find that only  $\sim 11$  per cent of the gas accreted by their simulated galaxies by  $z = 0$

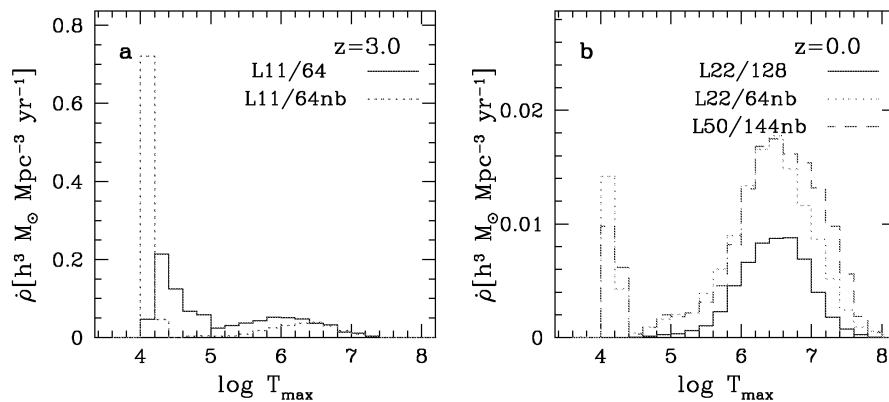


**Figure 11.** Influence of numerical resolution, simulation volume and the UV background on the  $T_{\max}$  distribution. (a) Comparison of L11/64 and L11/64nb, which differ only in the presence of a UV background, at  $z = 3$ ; (d) The volume effect comparisons of L22/128, L22/64nb and L50/144nb at  $z = 0$ .

was ever hotter than  $10^5$  K. We have recently analysed a simulation, kindly provided by L. Hernquist and V. Springel, that uses Springel & Hernquist's (2002) entropy-conserving formulation of SPH, which makes the numerical treatment of shock heating significantly different from that in our code. This simulation, run Q3 of Springel & Hernquist (2003b), represents a  $10 h^{-1}$  Mpc box with  $2 \times 144^3$  particles, and is evolved to  $z = 2.75$ . The simulation also includes strong feedback from stellar winds, using the methods described by Springel & Hernquist (2003a). Despite these differences in numerical method and input physics, the Springel & Hernquist (2003b) simulation produces a  $T_{\max}$  histogram at high redshifts that closely resembles those shown in Fig. 2, with a large fraction of gas accretion occurring at low temperatures. The transition between cold-mode dominance and hot-mode dominance occurs at a halo mass similar to that found in Fig. 6. However, the strong feedback makes galaxy baryonic masses significantly smaller in the Springel & Hernquist (2003b) simulation than in our simulation (numerical differences may also play a role), so the baryonic mass at which this transition occurs is lower than that in Fig. 5 by a factor of  $\sim 4$ . In summary, galaxy masses and the amount of accretion are lower in the Springel & Hernquist (2003b) simulation, but the existence of a cold accretion mode and the relative amounts of cold and hot accretion at a given halo mass appear entirely consistent with our results.

These internal and external comparisons strongly suggest that the bimodal  $T_{\max}$  histogram is a genuine physical result, at least given the physical assumptions of these simulations. As the results quoted above are all based on SPH simulations, albeit with different numerical implementations, it would be desirable to confirm the result with Eulerian grid or adaptive mesh hydrodynamic simulations, which typically use shock capturing methods instead of artificial viscosity to implement shock heating. Cen & Ostriker (1999; fig. 4) find a broad temperature distribution for cooling radiation in their Eulerian hydro simulation, suggesting that much of the gas in this simulation also cools without ever reaching  $T \geq 10^6$  K. A. Kravtsov (private communication), in adaptive mesh simulations of individual forming galaxies, finds that much of the gas penetrates along cold filaments far inside the virial radius without being shock heated. These simulations cannot presently measure the  $T_{\max}$  histogram itself because they do not track gas from cell to cell and therefore do not record the history of gas that ends up in galaxies, but this measurement can be carried out in the future by adding a population of 'tracer' particles that follows the gas flow (Kravtsov, private communication).

## 5 THE ENVIRONMENT DEPENDENCE OF ACCRETION AND STAR FORMATION RATE

Fig. 12 plots the globally averaged star formation rate and the globally averaged contributions of smooth accretion and mergers to galactic mass growth, as functions of time in the L22/128 simulation. At high redshifts the smooth accretion rate dominates the merging growth rate by a large factor, while at  $z < 1$  these two processes have comparable global rates. Of course, galaxies that gain most of their mass via mergers do exist in the simulation, but the growth of the typical galaxy is dominated by smooth accretion. MKHWD found that the global star formation history in the L50/144nb simulation closely tracks the gas accretion history and does *not* track the galaxy merger rate. Fig. 12 confirms this conclusion using our higher-resolution L22/128 simulation – the correlation between the accretion rate and SFR curves is even tighter than that found by

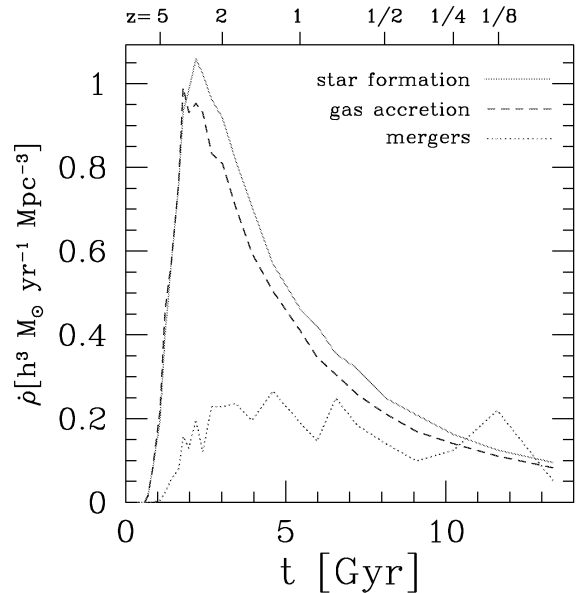


**Figure 12.** Star formation rate per unit comoving volume (solid line) for all resolved galaxies in the simulation compared with smooth gas accretion (dashed line) and merger accretion rates (dotted line). The merger mass accretion rates include total mass gain in merger events (gas and stars).

MKHWD. The two curves are offset by  $\sim 0.5$  Gyr, reflecting the average time that it takes gas to be converted into stars after it is accreted by a galaxy. However, with our observationally motivated assumption (e.g. Kennicutt 1998) that the star formation rate is an increasing function of gas density, any steadily accreting galaxy will form stars, and mergers are not needed as triggering events. Indeed, the global star formation rate must roughly track the global accretion rate for any star formation model in which galaxies do not build up large, quiescent gas supplies. Mergers could play a role in causing rapid bursts of star formation by driving galactic gas to higher densities, and our simulations may underestimate this effect because of their limited resolution. However, such merger-induced acceleration would have little effect on the globally averaged SFR because the merging galaxies simply consume the same amount of gas on a somewhat shorter time-scale.

If our input physics is approximately correct, then understanding the redshift and environmental dependence of the cold and hot accretion rates is tantamount to understanding the redshift and environmental dependence of galactic-scale star formation. In this section we focus on the environmental dependence; we return to the redshift dependence in Sections 6.3 and 6.4. Fig. 13 plots the mean SFR and accretion rate per galaxy as a function of environment, specifically the comoving space density of resolved galaxies computed using SPH-style kernel averaging on a galaxy-by-galaxy basis with a variable size spline kernel where the size is chosen to enclose 15 neighbours (as in Weinberg et al. 2004). The SFR and the accretion rate track each other as a function of density, just as the global rates track each other as a function of redshift. At  $z = 3$ , the average accretion rate is nearly independent of environment, but at lower redshifts there is a break towards lower accretion rates and star formation rates at  $n_{\text{gal}} \sim 1 h^3 \text{ Mpc}^{-3}$ . Points in Fig. 13 show the median accretion rate, computed in bins containing equal numbers of galaxies (while the mean is computed in bins of constant  $\Delta \log n = 0.2$ ). Comparing the medians and means, one can see that the accretion rate in high-density regions is dominated by the few

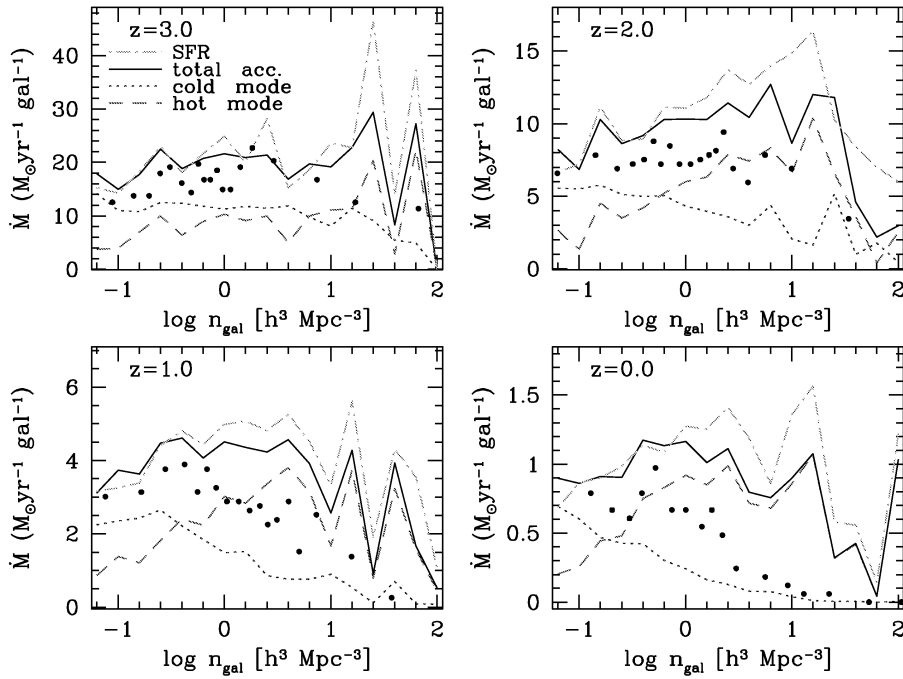


**Figure 13.** Dependence of accretion rates and star formation rates on the local galaxy number density (comoving), at  $z = 3, 2, 1$  and  $0$ . Solid lines show the mean total accretion rates in bins of  $\Delta \log n = 0.2$ , and dotted and dashed lines show the mean cold and hot contributions, respectively. Points show the median total accretion rate in bins containing equal galaxy numbers. Dot-dashed lines show mean star formation rates, which track the total accretion rate.

galaxies with large accretion rates; most galaxies in these regions have very low accretion and correspondingly low star formation.

The dotted and dashed lines in Fig. 13 show the separate contributions of cold and hot accretion to the mean accretion rate. There is a clear trend, increasingly pronounced at lower redshift, of cold-mode domination in low-density environments and hot-mode domination in high-density environments. The transition between the two modes shifts to progressively lower comoving densities at lower redshifts. The cold mode dominates in all but the highest-density environments at  $z \sim 3$ , but at  $z = 0$  it dominates only in the lowest-density environments and is insignificant at  $n_{\text{gal}} \gtrsim 1 h^3 \text{Mpc}^{-3}$ . These trends can be largely explained by the galaxy mass dependence of the cold-hot accretion fraction: low-density regions are populated by lower-mass galaxies, which tend to have more cold accretion. However, when we examine the trends separately for low- and high-mass galaxies, we find that there is also a direct environmental effect, in that low-mass galaxies are often hot-mode-dominated in high-density environments, while they are always cold-mode-dominated in low-density environments. This difference reflects the higher characteristic *halo* masses in dense environments; as noted in our discussion of Figs 5 and 6, low-mass galaxies in high-mass haloes tend to be hot-mode-dominated. The rare high-mass galaxies in low-density environments are still hot-mode-dominated, but they tend to have somewhat higher cold accretion fractions than those in denser regions.

We can compare our  $z = 0$  predictions to the results of Gómez et al. (2003, hereafter G03), who use  $H\alpha$  equivalent widths to infer the star formation rates of a volume-limited sample of galaxies from the SDSS. To mimic their selection of galaxies above an absolute magnitude limit  $M_r^* + 1$ , we choose galaxies above a baryonic mass threshold that yields the same galaxy number density, roughly the 120 most massive galaxies in our  $22.222 h^{-1} \text{Mpc}$  box. Like G03, we calculate the surface density around each galaxy by find-

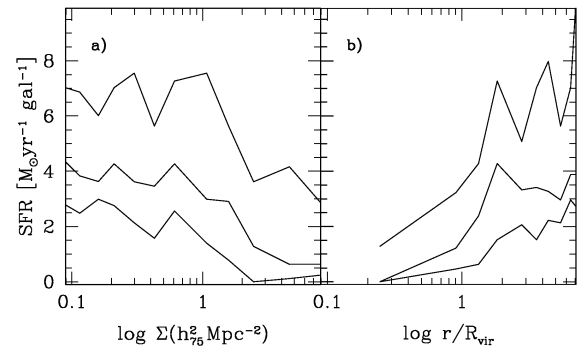


**Figure 14.** (a) Star formation rate versus the galaxy surface density at  $z = 0$ . Curves show the 25th percentile, median and 75th percentile of the SFR per galaxy in bins of surface density. (b) Same as (a), but galaxies are binned as a function of distance from the centre of the largest cluster in the L22/128 simulation, in units of the virial radius of the cluster.

ing the distance  $r_{10}$  to the tenth nearest neighbour in projection,  $\Sigma = 10/(\pi r_{10}^2)$ , after eliminating galaxies further than  $\pm 1000 \text{ km s}^{-1}$  in redshift (making use of our periodic boundary). To improve our statistics, we combine the results from the three orthogonal projections of the box.

Fig. 14(a) plots the median star formation rate and the 25th and 75th percentiles of the SFR distribution in bins of galaxy surface density containing equal number of galaxies, similar to fig. 4 of G03. The simulation reproduces the principal qualitative result of G03; namely, a break in the SFR versus  $\Sigma$  relation at  $\Sigma \sim 1 h_{75}^2 \text{Mpc}^{-2}$ , most prominent for the 75th percentile curve, with a slowly increasing SFR below the break and a rapidly declining SFR at higher surface densities. G03 also examine the dependence of SFR on the distance to the centre of the nearest group or cluster. They emphasize

that the break in SFR occurs at three to four times the cluster virial radius, implying that it is not an effect associated with virialization or the intracluster medium. We have just one prominent cluster in the L22/128 simulation, with virial mass  $2.7 \times 10^{14} M_{\odot}$ . Fig. 14(b) plots SFR against the projected distance to the centre of this cluster (defined by the position of the most bound particle), in units of the cluster virial radius  $R_{\text{vir}} = 1.1 h^{-1} \text{ Mpc}$ , for comparison to G03's fig. 6. The breaks in the simulated SFR curves also occur beyond the cluster virial radius, at roughly  $2R_{\text{vir}}$ . At least part of the drop at large radii is caused by the presence of a large galactic group at distances between 1 and  $2R_{\text{vir}}$ , which dominates the statistics. A more detailed comparison would require a larger simulation volume that would allow us to mimic G03's group selection method more carefully. As the SFR tracks the gas accretion rate in our simulations, a drop in SFR within high-density regions at low redshifts is a direct consequence of a diminished gas supply and does not require cluster-specific processes that either rapidly consume the existing gas (e.g. galaxy harassment) or remove it from galaxies (e.g. ram pressure stripping).

G03 note that their SFR values should be multiplied by a factor of  $\sim 5$  to account for the 3-arcsec aperture of the SDSS fibres, but even so they are significantly lower than the rates predicted by the simulation. For example, the plateau of the 75th percentile SFR curve is at  $\sim 2 M_{\odot} \text{ yr}^{-1} \text{ gal}^{-1}$  in G03 (including the factor of 5) and  $\sim 5 M_{\odot} \text{ yr}^{-1} \text{ gal}^{-1}$  in the simulation. The 25th percentile curve is consistent with zero SFR at all  $\Sigma$  in G03, while the simulation predicts 25th percentile rates  $\sim 1.5 M_{\odot} \text{ yr}^{-1} \text{ gal}^{-1}$  in low-density environments. G03 include negative estimates of the SFR derived from H $\alpha$  flux in their median calculation, which slightly lowers their SFR values, but probably not by a large factor. Limited mass resolution of our simulation may have some effect in making the predicted SFR and accretion rates artificially high (see Section 4.3). In any event, we are encouraged that the simulation reproduces one of the most striking features of the observed correlation between SFR and environment, a break at surface densities of  $\sim 1 h_{75}^2 \text{ Mpc}^{-2}$  that lie beyond the virial radii of rich galaxy groups, a result found independently by G03 in the SDSS and by Lewis et al. (2002) in the 2dF Galaxy Redshift Survey. (The SDSS results of Kauffmann et al. 2004 also appear to be consistent with this finding, although they do not present them in this form.) This break occurs in a density regime where the accretion rates are dominated by the hot mode (see Fig. 13), and galaxies above G03's  $M_{*}^{*} + 1$  threshold are mostly hot-mode-dominated in any case. Thus, although these observations test some aspects of the simulation predictions, they do not test the existence of an important cold accretion mode or the transition of the dominant accretion mode from cold to hot with increasing galaxy density. Such effects should become more apparent if the galaxy sample is extended to include lower-luminosity systems.

## 6 DISCUSSION

### 6.1 Physics of the hot mode

In our simulations, hot accretion ( $T_{\text{max}} > 2.5 \times 10^5 \text{ K}$ ) dominates over cold accretion in galaxies of baryonic mass  $M_{\text{gal}} \gtrsim 10^{10.3} M_{\odot}$  (Fig. 5) or in haloes with  $M_{\text{halo}} \gtrsim 10^{11.4} M_{\odot}$  (Fig. 6). Roughly half of the total baryonic mass of high-mass galaxies ( $M_{\text{gal}} \gtrsim 10^{11} M_{\odot}$ ) originates from hot accretion, while lower-mass galaxies are built predominantly by cold accretion (Fig. 7). The hot accretion mode in the simulations corresponds reasonably well to the accretion envisioned in the standard picture of galaxy formation that underlies most semi-analytic models: gas shock heats to roughly the halo

virial temperature before cooling and settling into a galaxy (Rees & Ostriker 1977; Silk 1977; White & Rees 1978; White & Frenk 1991).

The actual distribution of  $T_{\text{max}}/T_{\text{vir}}$  for hot-mode accretion is broad, roughly an order of magnitude (Fig. 3). This broad distribution reflects a combination of departures from spherical symmetry, hierarchical assembly and post-virialization heating. With aspherical infall, gas can hit an accretion shock with a range of velocities and thus heat to different temperatures. Some gas may be shocked to  $T_{\text{max}} < T_{\text{vir}}$  in filamentary structures beyond the virial radius and then enter the halo without experiencing a true virial shock. When an individual galaxy falls into a group or cluster, some of its halo gas is heated to the higher virial temperature of the new halo and escapes the galaxy potential well, but other gas remains at the virial temperature of the galaxy and may be accreted before it is heated or stripped. As we calculate the ratio of  $T_{\text{max}}$  to the virial temperature of the host halo of a galaxy at the time of accretion, hot-mode gas accreted in this way will also have low  $T_{\text{max}}/T_{\text{vir}}$ . Finally, gas that heats by an accretion shock near the virial radius can be heated further by adiabatic compression as it flows inwards and increases its density. We find that a significant fraction of the hot-mode gas has  $T$  significantly below  $T_{\text{vir}}$  (but still much higher than the typical cold-mode temperature) in the outer regions of the halo and does not reach  $T_{\text{vir}}$  until it is inside  $\sim 0.5R_{\text{vir}}$ .

Fig. 15 shows the same  $\rho$ - $T$  trajectories as Fig. 1(b), but now the horizontal axis represents physical density (scaled to the mean baryon density at  $z = 3$ ) rather than overdensity. In this plane, adiabatic compression moves a particle along a line  $\log T \propto (2/3) \log \rho$ . In the diffuse IGM phase, particles move to lower densities and temperatures as the universe expands, along a locus of slope close to 0.6. Hot-mode particles then experience sudden shock heating, which is often followed by an extended phase of heating along a nearly adiabatic trajectory, before eventually cooling to  $10^4 \text{ K}$  and

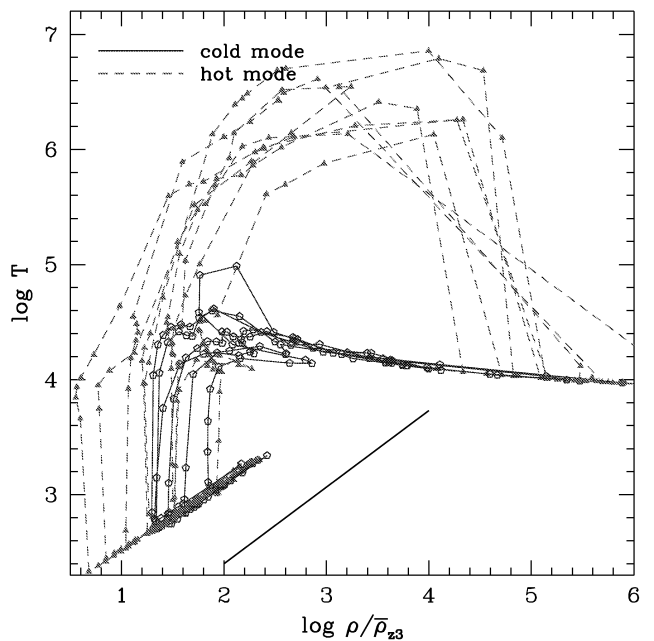


**Figure 15.** Density–temperature trajectories for the same particles shown in Fig. 1(b), but with the horizontal axis representing the physical density (scaled to the cosmic mean density at  $z = 3$ ) instead of the overdensity. The line segment at the bottom has the slope  $d \log T / d \log \rho = 2/3$  expected for pure adiabatic evolution.



high overdensity. The fact that shock heating is spread over several outputs (which are typically spaced by  $\sim 0.05\text{--}0.1$  Gyr) is a consequence of the finite numerical width of the shocks. We will discuss the behaviour of cold-mode particles in this plot below.

We have also examined the distribution of cooling times in haloes at various redshifts. If we calculate the amount of hot gas that would cool between two outputs in the absence of further heat input, we obtain a value that exceeds the actual hot-mode accretion rate by a factor of  $\sim 2$ . Therefore, adiabatic compression or further shock heating must be sufficient to prevent roughly half of this gas from cooling.

## 6.2 Physics of the cold mode

Why does a substantial fraction of gas enter galaxies without ever heating close to the virial temperature of the parent dark matter halo of the galaxy? Our results do not provide a comprehensive answer to this question, but they do offer a number of clues that allow us to build a physical picture of how cold accretion occurs. As discussed in Section 3, the division between hot and cold modes occurs at roughly constant  $T_{\max}$  rather than constant  $T_{\max}/T_{\text{vir}}$ , which suggests that it is determined mainly by cooling physics rather than by shock heating. The strong dependence of the  $T_{\max}$  distribution for cold-mode gas on the presence of a UV background (Fig. 11) further supports this inference. The ratio of cold to hot accretion is tightly correlated with galaxy mass or halo mass, and the transition between cold-mode dominance and hot-mode dominance occurs close to (though somewhat above) the halo mass predicted by the spherically symmetric models of Birnboim & Dekel (2003). The ratio of cold to hot accretion also depends on the density of the environment, at least at low redshift, and although this dependence largely reflects the relative galaxy mass functions in high- and low-density regions, low-mass galaxies are dominated by hot accretion in high-density environments and by cold accretion in low-density environments.

The trajectories of particles in the  $\rho\text{--}T$  plane offer further insight into the physics of cold accretion. Fig. 1(b) shows that typical cold-mode particles, after an initial phase of adiabatic cooling, experience most of their heating at overdensities of  $\sim 3\text{--}30$ , and then steadily increase their overdensity while cooling from slightly above  $10^4$  to  $10^5$  K. Fig. 15, plotted in physical density rather than overdensity, shows that the heating phase of these trajectories is very steep, implying that it is produced by shocks not by adiabatic compression. The characteristic shock velocities must be  $v \sim (kT/\mu m_p)^{1/2} \sim 10\text{--}35$  km s $^{-1}$  ( $T \sim 10^4\text{--}10^5$  K) and are probably around filaments.

To better understand the origin of the hot–cold distinction, it is useful to look for differences in the physical state of gas *before* it is accreted in one of these two modes. Fig. 16 plots the average overdensity and temperature histories of gas that is accreted on to galaxies at  $z = 2$ . Solid lines show histories for cold-mode particles and dashed lines for hot-mode particles. Averaging over many particles tends to smooth the density and temperature evolution, as individual particles experience their rapid heating phases at different times. The important result in Fig. 16 is that cold-mode particles initially have higher overdensities than hot-mode particles, at least on average. Because of the correlation between density and temperature in the photoionized IGM (Fig. 1), cold-mode particles also start at a slightly higher temperature. The differences are fairly small, and become somewhat larger if we focus only on the lower- $T_{\max}$  cold-mode particles. The general appearance of Fig. 16 is similar at other redshifts.

As overdensities of  $\sim 3\text{--}30$  are associated with filamentary structures, while halo overdensities are  $\gtrsim 100$ , these  $\rho\text{--}T$  trajectories suggest that cold-mode particles experience much of their heating in filamentary structures, while hot-mode particles are heated at halo virial shocks. Fig. 17 provides anecdotal evidence to support this idea. The left-hand panels show an example of a cold-mode-dominated halo ( $M_{\text{halo}} = 2.6 \times 10^{11} M_{\odot}$ ) containing a well-resolved galaxy ( $M_{\text{gal}} = 1.6 \times 10^{10} M_{\odot} \approx 10000 m_{\text{SPH}}$ ) in the L5.5/128 simulation at  $z = 5.52$ . The right-hand panels show this same halo and its surroundings at  $z = 3.24$ , when it is well into the hot-mode-dominated regime ( $M_{\text{halo}} = 1.26 \times 10^{12} M_{\odot}$ ,  $M_{\text{gal}} = 7.35 \times 10^{10} M_{\odot}$ ). Particles are colour coded by overdensity in the upper panels and by temperature in the middle panels, all of which are  $4 R_{\text{vir}}$  on a side and  $2 R_{\text{vir}}$  thick. The lower panels show a zoomed region of the temperature plot,  $1 R_{\text{vir}}$  on a side and  $0.5 R_{\text{vir}}$  thick. Lines attached to particles show their projected velocities. In the left-hand panels, green particles represent cold-mode gas that will be accreted by the central galaxy by  $z = 5$ , 130 Myr later. In the right-hand panels, they show hot-mode gas that will be accreted by  $z = 3$ , 190 Myr later.

The  $z = 3.24$  picture corresponds reasonably well to the conventional notion of galactic gas accretion, with accreting material coming from the inner regions of a hot, quasi-spherical halo. However, even at this redshift cold filaments penetrate fairly far inside the halo, where they heat up to higher temperatures. The cold-mode accretion at  $z = 5.52$ , in contrast, is clearly directed along the intersecting filaments, and this coherent filamentary flow allows the galaxy to accrete gas from larger distances. A. Kravtsov (private communication) finds similar behaviour in adaptive mesh simulations of an individual galaxy: the forming galaxy is surrounded by

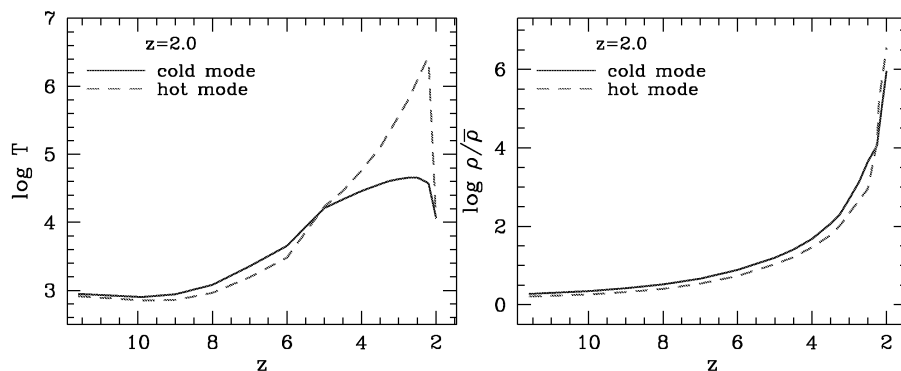


**Figure 16.** The average temperature (left-hand panel) and density (right-hand panel) evolution of cold-mode (solid line) and hot-mode (dashed lines) particles that are accreted on to galaxies at  $z = 2$ .

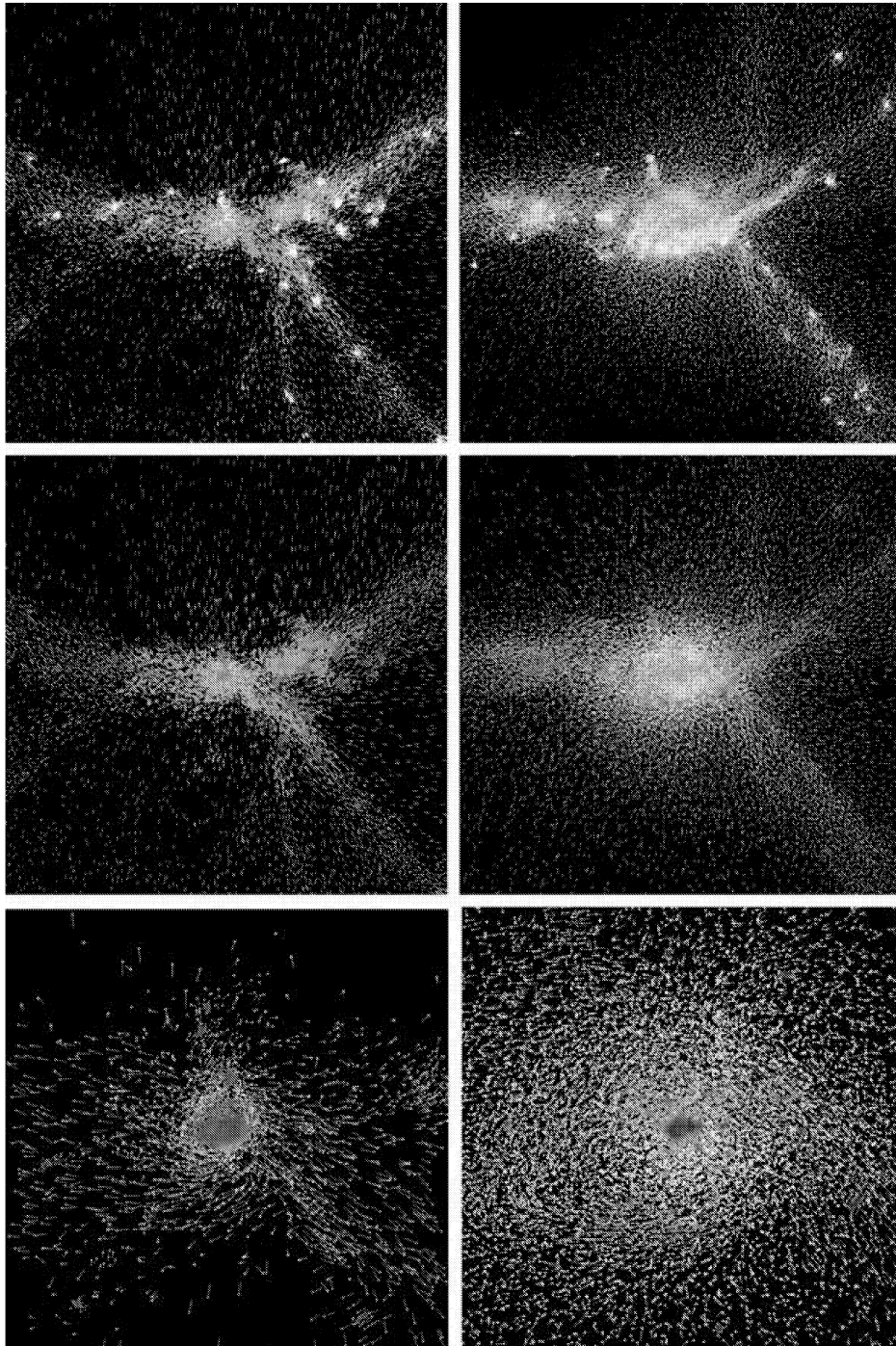


**Figure 17.** Accretion pattern around the largest galaxy in the L5.5/128 simulation. Left-hand panels show redshift  $z = 5.52$ , when the galaxy baryonic mass is  $1.6 \times 10^{10} M_{\odot}$  and accretion is almost entirely dominated by the cold mode. Green particles in each panel represent gas that will be accreted in the cold mode by  $z = 5$ . Right-hand panels show redshift  $z = 3.24$ , when the galaxy mass is  $7.35 \times 10^{10} M_{\odot}$  and accretion is almost entirely dominated by the hot mode. Green particles in these panels show gas that will be accreted in the hot mode by  $z = 3$ . Other particles in the top panels are colour coded by overdensity, from 0.67 (darkest blue) to  $>2000$  (white), in a region  $4 R_{\text{vir}}$  on a side ( $78 h^{-1} \text{ kpc}$  and  $202 h^{-1} \text{ kpc}$  in physical units at  $z = 5.52$  and  $3.24$ , respectively) and  $2 R_{\text{vir}}$  thick. Other particles in the middle panels are colour coded by temperature in the same region. The temperature scale starts from the lowest temperature (darkest blue) 1500 K on the left and 3000 K on the right-hand panels, to the highest temperature (white);  $5 \times 10^6$  K on the left and  $10^7$  K on the right-hand panels. The bottom panels have the same temperature colour-coding but zoom in to show a region  $1 R_{\text{vir}}$  on a side and  $0.5 R_{\text{vir}}$  thick. Vectors attached to particles show their projected velocities.

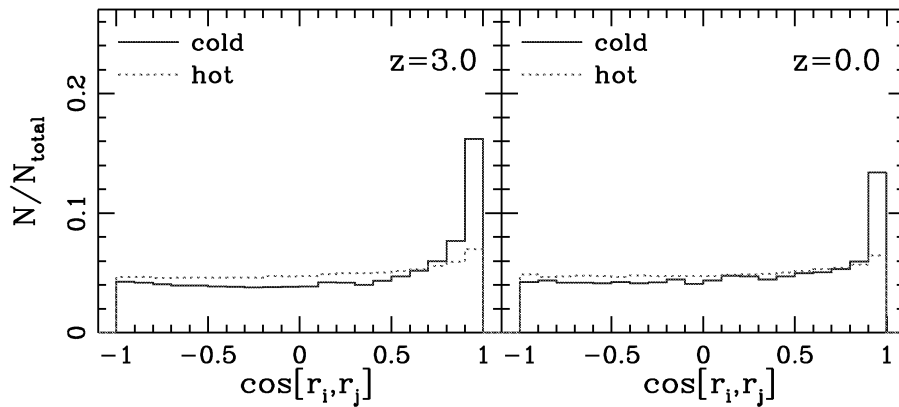


**Figure 18.** The distribution of the normalized scalar products of the radius vectors of accreting particles (see the text) at the indicated redshifts. The dotted histogram is the hot mode and the solid histogram is the cold mode.

a hot gas halo, but cold filaments with coherent flows penetrate far inside this halo. The cluster scale simulations of Nagai & Kravtsov (2003) do not include gas cooling, but they still show filamentary structures in which the gas entropy is far below that of the surrounding, spherically distributed gas.

To quantify the evidence for filamentary cold accretion, we applied the following test. First, at the redshift output before the accretion output we find the radial vectors  $\mathbf{r}_i^g$  connecting the centre of each resolved galaxy  $g$  to the positions of all particles  $i$  that it will accrete. Next, we determine the normalized scalar product  $\hat{\mathbf{r}}_i^g \cdot \hat{\mathbf{r}}_j^g = \cos[\mathbf{r}_i^g, \mathbf{r}_j^g]$  for pairs of particles that accrete on to the same galaxy  $g$ . We compute the distribution of  $\cos[\mathbf{r}_i^g, \mathbf{r}_j^g]$  separately for all pairs of hot-mode particles and all pairs of cold-mode particles, summing the distributions for all galaxies  $g$  and normalizing them to unity. Fig. 18 shows the results at  $z = 3$  and 0.

Hot-mode particles show a nearly uniform distribution of  $\cos[\mathbf{r}_i^g, \mathbf{r}_j^g]$ , which is expected for a statistically isotropic accretion pattern. Cold-mode particles, in contrast, show a strong peak at  $\cos[\mathbf{r}_i^g, \mathbf{r}_j^g] \approx 1$ , indicating accretion from preferred directions, i.e. along filamentary structures. The size of this peak underestimates the fraction of accretion that is filamentary, as particle pairs accreting from different filaments that feed the same galaxy produce  $\cos[\mathbf{r}_i^g, \mathbf{r}_j^g]$  peaks at other angles, and averaging over the full galaxy population turns these multiple peaks into a uniform spread. Also, filaments are not perfectly straight, and they have a finite geometrical cross-section, both of which tend to spread the  $\cos[\mathbf{r}_i^g, \mathbf{r}_j^g]$  values. None the less, this test shows a clear statistical difference in the geometry of cold and hot accretion, consistent with the visual impression of Fig. 17. If we remake these plots separately for haloes above and below  $M = 2 \times 10^{11} M_\odot$ , we find that the directional signal in the cold accretion mode is stronger for high-mass haloes and weaker for low-mass haloes, while hot accretion remains approximately isotropic in both regimes. Some of the difference between low- and high-mass haloes could be numerical in origin, but we believe that it primarily reflects a more isotropic nature of cold accretion in low-mass systems.

From these clues, we can build the following picture of cold accretion. As argued by Binney (1977) and Birnboim & Dekel (2003), accreting gas with short cooling times does not form a classic virial shock – its effective equation of state is too soft, and it passes through the virial radius essentially in free fall. In the spherically symmetric models of Birnboim & Dekel (2003), there is a sharp transition between low-mass haloes that do not have a virial shock and high-mass haloes that do, with the approximate condition being that a

virial shock arises if the post-shock cooling time is larger than the dynamical time. The important new ingredient highlighted by the simulations is the filamentary nature of cold accretion. Departures from spherical symmetry allow galaxies to have a mix of cold and hot accretion at one time, so the sharp transition of the Birnboim & Dekel (2003) models is replaced by a steady change from cold-mode domination at low mass to hot-mode domination at high mass. A low-mass galaxy has no virial shock anywhere, so it can accrete cold gas quasi-spherically, though filaments still channel much of the flow. An intermediate-mass galaxy has a virial shock everywhere except at the points where dense filaments of cold gas penetrate the virial radius. These galaxies have a mix of cold, filamentary accretion and hot, quasi-spherical accretion. Gas in denser regions of the IGM is more likely to join a filament before accreting on to a galaxy, explaining the difference of density histories in Fig. 16. Finally, high-mass galaxies have a virial shock everywhere and have only hot accretion.

The characteristic halo mass at which we find equal cold and hot accretion rates,  $M \sim 3 \times 10^{11} M_\odot$ , is a factor of  $\sim 2$ – $3$  larger than the transition mass calculated by Birnboim & Dekel (2003). However, Dekel & Birnboim (2005) show that the derived transition mass depends on the precise criterion they use, in particular the radius at which they require a shock to form. For low-metallicity gas, they find a transition mass of  $\sim 1.5 \times 10^{11} M_\odot$  for a shock at  $0.1 R_{\text{vir}}$  and  $\sim 10^{12} M_\odot$  for a shock at  $R_{\text{vir}}$ , though the addition of a UV background (as used here) would lower cooling rates and probably reduce these masses. Given the radical difference in calculational methods, the agreement between the SPH simulations and the spherically symmetric models is remarkably good, pointing to similar underlying physics.

Semi-analytic models of galaxy formation distinguish between accretion with long post-shock cooling times, in which the cooling radius is smaller than the halo virial radius, and accretion with rapid post-shock cooling, in which the cooling radius exceeds the virial radius (White & Frenk 1991). In both cases, the cooling time is calculated assuming shock heating to the virial temperature, but in the latter case the gas is assumed to accrete on to the central galaxy at the free-fall rate instead of first forming a hot atmosphere in quasi-hydrostatic equilibrium. We have calculated the halo mass that marks the transition between these two cases for our adopted cosmology and cooling function, including the effects of the UV background. We calculate cooling radii assuming that halo gas follows an NFW density profile (Navarro, Frenk & White 1996) reduced by  $\Omega_b/\Omega_m$ , and we take typical concentrations as a

function of redshift from Bullock et al. (2001a). If we define the cooling radius to be the radius at which the cooling time equals  $t(z)$ , the age of the universe at redshift  $z$ , then we find a transition mass  $\sim 7 \times 10^{10} M_{\odot}$  at  $z \gtrsim 1.0$ , roughly two to four times lower than the transition mass found in our simulations. At  $z < 1.0$  there is no transition mass at all; in the presence of a UV background, the cooling radius never exceeds the virial radius at the lower densities that prevail in low-redshift haloes. If we use either the free-fall time or the average dynamical time of the halo to define the cooling radius then the transition mass at high redshift is reduced by another factor of 2–4, and there is no transition mass at  $z \lesssim 3$  and 2.5. Thus, while the cooling radius transition in existing semi-analytic models bears a qualitative resemblance to the cold–hot transition identified in this paper, a standard calculation of this transition yields a result that is quantitatively different and underestimates the significance of cold accretion (see the Appendix for details of our calculation). The transition mass goes up if one ignores the UV background (thus raising the cooling rates) or assumes an  $r^{-2}$  gas density profile (thus raising the density at the virial radius), but the first of these assumptions ignores a physical process present in the simulation, and dark matter profiles, at least, are much better described by NFW profiles than by isothermal spheres. The cooling radius approach also fails to capture the filamentary nature of cold accretion, and because the cooling radius is calculated assuming virial temperature gas, it implicitly predicts that most of the emission from even rapidly cooling gas will be at the X-ray wavelengths characteristic of these temperatures, while in the simulations this gas radiates much of its energy in atomic line transitions, hydrogen Ly $\alpha$  in particular (Fardal et al. 2001). The exact amount of radiated Ly $\alpha$  emission, however, needs further investigation, as it could be partially affected by the numerical broadening of shocks.

One question remains: how does cold-mode gas actually enter a galaxy? Our ability to answer this question is limited because our simulations do not have good enough resolution at the relevant scales, but we know that gravitational infall to galaxy mass potential wells produces typical inflow velocities of  $\sim 100$ – $300 \text{ km s}^{-1}$ , and something must happen to the corresponding kinetic energy. (The simulation code conserves energy, so it cannot be lost to numerical effects.) We can identify three possibilities, all of which may operate to some degree. First, gas could penetrate inside the virial radius but be stopped by a strong shock close to the galaxy disc, heating to the virial temperature and converting its infall energy to thermal energy. The post-shock cooling time is then very short because the gas density near the disc is high. Some particles in our simulations exhibit exactly this behaviour and A. Kravtsov’s adap-

tive mesh simulations also show shock heating far inside the virial radius at the terminations of cold filamentary flows (A. Kravtsov, private communication). The lower left-hand panel of Fig. 17 shows some examples of such particles, with temperatures near  $T_{\text{vir}}$  in a quasi-spherical region of several kpc around the central galaxy.

We formally count such particles as hot-mode accretion, as they have a high  $T_{\text{max}}$ , but physically they are more analogous to cold-mode particles, as they do not shock heat near the virial radius. Because of our finite time resolution, we miss the heating events for some of these particles and actually count them as being cold mode. However, we think it is unlikely that *most* of the particles we identify as cold mode experience this kind of strong shock heating near the galaxy disc, in part because improving the time resolution makes only a small difference to the fraction of cold-mode particles (Section 4.2) and in part because of the cooling radiation arguments of Fardal et al. (2001): the total amount of energy radiated by accreting gas is of the order of the gravitational binding energy, and a large fraction of this energy emerges from low-temperature gas. However, it is possible that high-density accretion shocks near the forming disc are more common in the real Universe and are missed in our simulations because of their finite spatial resolution.

A second possibility is that cold-mode gas smoothly merges on to the galaxy disc like a stream of cars entering an expressway, converting its infall velocity to rotational velocity. This idea may seem outlandish at first, but the disc acquires its angular momentum from the accreting gas, so the required alignment of the disc with the accretion flow may arise naturally. The large-scale filamentary structure around galaxies persists for long periods of time, especially at high redshifts where the galaxies are highly biased with respect to the dark matter. A close examination of galaxies in our highest-resolution simulation provides some evidence for this expressway mechanism, as one can see visually in the lower left-hand panel of Fig. 17, but further analysis will be needed to assess its overall importance. In any event, the virial theorem suggests that this mechanism could provide only part of the energetic solution, as the rotational energy of the galaxy should be smaller than its gravitational binding energy. (Note, however, that the virial theorem cannot be applied with precision to non-isolated, time-dependent systems such as forming galaxies, and the bookkeeping is further complicated by the fact that dark matter dominates the gravitational potential.)

The third possibility is that infalling cold-mode gas is slowed either adiabatically (i.e. by pressure gradients) or in a series of shocks that are individually too weak to cause strong heating. The left-hand panel of Fig. 19 plots the average radial infall velocity of cold-mode

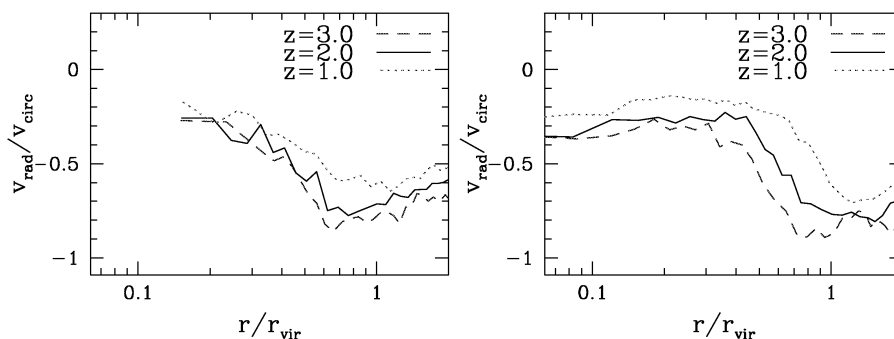


**Figure 19.** Left: the median radial velocity of cold-mode gas before it is accreted as a function of galactocentric radius. Radii are scaled to the halo virial radius,  $r_{\text{vir}}$ , and velocities to the halo circular velocity,  $v_{\text{circ}}$ . Results are shown at  $z = 1.0$  (accreted by  $z = 0.0$ , dotted),  $z = 2$  (accreted by  $z = 1.0$ , solid) and  $z = 3$  (accreted by  $z = 2.0$ , dashed). We only consider gas accreted on to the central galaxies of their parent dark matter haloes. Right: the same for hot-mode particles.

gas, scaled to the halo circular velocity, as a function of  $r/r_{\text{vir}}$ . We only consider cold-mode gas that will be accreted on to the central galaxies by the next indicated redshift. We define the central galaxy as the most massive galaxy in the halo, which is almost always the galaxy closest to the halo centre. We show results at  $z = 3$  (dashed line, accreted by  $z = 2$ ),  $z = 2$  (solid line, accreted by  $z = 1$ ) and  $z = 1$  (dotted line, accreted by  $z = 0$ ). Near the virial radius, the average infall velocity is similar to the halo circular velocity, but starting at  $r \sim 0.5 R_{\text{vir}}$  the gas decelerates smoothly, and by  $r \sim 0.1 R_{\text{vir}}$  the average infall velocity is only 10–20 per cent of the circular velocity. The mean infall pattern is similar at all three redshifts, with the trend that the normalized velocities are lower at lower redshifts. There is a large scatter about the mean velocity, so some accreting particles must either shock heat near the disc or join the rotational flow as discussed above. However, based on Fig. 19, we tentatively conclude that deceleration by pressure gradients or weak shocks is the primary mechanism by which cold-mode gas loses its infall velocity, at least in the simulations, radiating its dissipated energy as it slows. Artificial cooling of gas in numerically broadened shocks (see Section 4.3) could have some effect on this result, at least in its quantitative details.

In contrast, the right-hand panel of Fig. 19 shows the situation for hot-mode particles. We see that hot-mode accretion more closely resembles the standard picture where the gas slows rapidly at a shock near the virial radius. However, the zone where the gas slows down is significantly inside the virial radius at  $z = 3$  (at  $\sim 0.6 R_{\text{vir}}$ ) and moves steadily towards  $R_{\text{vir}}$  by  $z = 0$ . Furthermore, this zone is fairly broad, and the post-shock gas still has a mean radial velocity that is a significant fraction of  $v_{\text{circ}}$ , especially at high  $z$ . These complications reflect the departures from spherical symmetry and equilibrium discussed in Section 6.1. Although hot accretion shows no significant filamentary signal in Fig. 18, from visual inspection we see that even in some of the biggest haloes at high redshift a large fraction of the accreted gas comes from filaments. Filaments in these haloes are hot (with temperatures well above the cold-mode limit) but with temperatures much lower than  $T_{\text{vir}}$ . These filaments and mergers can deliver hot gas (and cold) well inside  $R_{\text{vir}}$ , with significant radial velocity. Haloes at low redshift have better developed virial shocks and clearer separations from their filamentary surroundings, and the standard picture becomes a better approximation.

Further numerical investigations should significantly improve our physical understanding of cold accretion. Birnboim & Dekel (2003) and Dekel & Birnboim (2005) argue that the physical criterion that determines whether a virial shock forms in their spherically symmetric calculations is the ratio of the cooling time to the ‘compression time’ under post-shock conditions. In future work, we will investigate whether this condition works as a *local* criterion for strong shock heating in our simulations. Our comparison of simulations with and without a UV background already points to an important role for cooling rates, and comparison of simulations with primordial and metal-line cooling and with different choices of  $\Omega_b$  and  $\Omega_m$  will help unravel the factors that determine the cold-hot transition mass. Most valuable will be very high-resolution simulations that can accurately follow cold accretion streams all the way into galaxy discs, preferably performed with both SPH and adaptive mesh methods.

### 6.3 Connection to global star formation and galaxy structure

As shown in Fig. 12, the cosmic star formation rate drops by a factor of  $\sim 11$  from  $z = 3$  to 0. Unfortunately, this star formation history

cannot be directly compared with observations because none of our current simulations has the dynamic range to include all the galaxies that contribute significantly to the global star formation rate at all redshifts. In a forthcoming paper (Fardal et al., in preparation), we carefully combine the results from several simulations that span a range of volume sizes and resolutions to determine a global rate that can fairly be compared with the observational results. We find that the global SFR is approximately constant from  $z = 6$  to 2, and then drops by a factor of 12 from  $z = 2$  to 0. The simulation predictions are consistent with the observations within their scatter, but this is not a stringent test because the observational estimates themselves span a wide range of values at any one redshift.

As the history of the cosmic star formation rate in our simulations closely tracks the history of gas accretion, as shown in Fig. 12, to understand the evolution of the cosmic star formation rate it is sufficient to understand the evolution of the smooth gas accretion rate. From Fig. 4 we see that both the cold and hot accretion rates decline at  $z < 2$ , with the cold-mode decrease starting earlier and occurring more rapidly. As already discussed in Section 3, the transition in the global accretion rate from cold-mode-dominated at high redshift to hot-mode-dominated at low redshift simply reflects the increasing mass scale of galaxies and haloes, as low-mass systems are cold-mode-dominated and high-mass systems are hot-mode-dominated at every redshift. However, the drivers of the declining accretion rate are somewhat different in the two cases.

First, let us concentrate on the drop in the global cold-mode accretion rate. In principle, this could reflect a decrease in the space density of cold-mode galaxies or a decrease in the amount of cold-mode accretion per galaxy, or a combination of the two. The rapid rise seen in Fig. 4 reflects the increasing space densities of galaxies above our mass resolution threshold; most of these galaxies are cold-mode-dominated at high redshift. However, while the space density of cold-mode galaxies peaks at  $z \sim 2$ , it declines only very slowly thereafter. Most of the decline in cold-mode accretion must therefore be driven by the declining accretion rate per galaxy, as shown directly in Fig. 20, which plots the average gas accretion rate

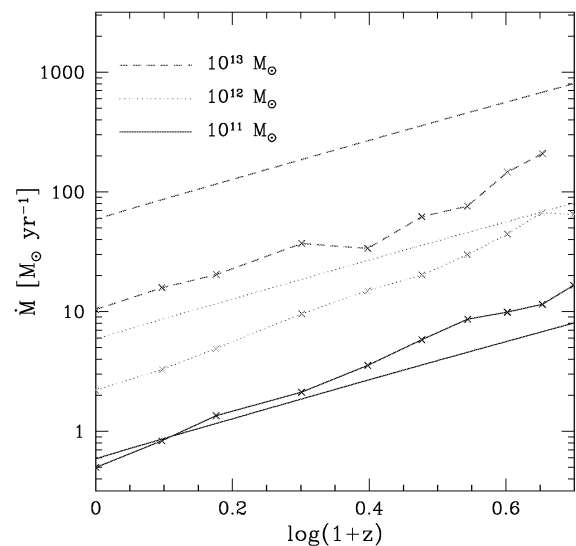


**Figure 20.** The average gas accretion rate on to the central galaxies of haloes with  $\log M_{\text{vir}}/M_{\odot} = 11 \pm 0.1$  (solid lines),  $\log M_{\text{vir}}/M_{\odot} = 12 \pm 0.15$  (dotted lines) and  $\log M_{\text{vir}}/M_{\odot} = 13 \pm 0.15$  (dashed lines), as a function of redshift. Lines marked with crosses show results from the L22/128 simulation, while smooth, unmarked lines show the analytical infall models described in the text.

on to the central galaxy in haloes of different masses as a function of redshift. For haloes in the mass range  $\log M_{\text{vir}} = 11 \pm 0.1 M_{\odot}$ , which is cold-mode-dominated at every redshift, the mean accretion rate per galaxy drops by a factor of  $\sim 12$  between  $z = 2$  and 0, accounting for the drop in the global cold-mode accretion rate.

The smooth solid curve in Fig. 20 shows the prediction of a simple analytical model along the lines of White & Frenk (1991): the accretion rate is just  $\dot{M} = f_{\text{g}} \dot{M}_{\text{vir}}$  where  $f_{\text{g}}$  is the universal gas fraction (i.e. the universal baryon fraction minus the fraction of baryonic mass in stars) and  $\dot{M}_{\text{vir}} = (4\pi/3)R_{\text{vir}}^3 \dot{\rho}_{\text{vir}}$  is the virial mass. The change in virial mass  $\dot{M}_{\text{vir}}$  is determined through the cosmological growth of the virial radius assuming an isothermal profile, fixed circular velocity and the cosmological evolution of  $\rho_{\text{vir}}$ . For  $10^{11} M_{\odot}$  haloes, this model explains the simulated accretion rates quite well. One can view the steady decline of  $\dot{M}$  as a consequence of the declining density at the virial radius, which is tied to the declining mean density of the Universe, or of the corresponding increase in characteristic dynamical times – the time for a halo to double its mass scales with the age of the Universe.

At high redshifts the analytical model underpredicts the accretion rate by a factor of  $\sim 2$ , for at least two reasons. First, much of the accretion is filamentary, allowing haloes to draw material from beyond the virial radius and to accrete more efficiently than a spherical model predicts. Secondly, haloes in this mass range are only  $\sim 2$  times our resolution limit, and we are biased towards including haloes that have higher accretion rates because we only count haloes that have already formed a resolved central galaxy. This effect operates at all redshifts, but it is more important at high redshifts when galaxies have had less time to grow, causing us to omit lower  $\dot{M}$  galaxies from our average. In addition, our limited mass resolution may play some role in overestimating accretion rates. When we repeat the  $\dot{M}$  analysis for the higher-resolution L11/128 simulation at  $z = 3$  and 4, the mean accretion rate is lower and agrees even better with the analytical model, though the rate is still higher by  $\sim 20$  per cent at  $z = 3$  and  $\sim 40$  per cent at  $z = 4$ .

Crosses connected by dotted and dashed lines in Fig. 20 show the mean accretion rates for the central objects of more massive haloes, with  $\log M_{\text{vir}}/M_{\odot} = 12 \pm 0.15$  and  $13 \pm 0.15$ , respectively. Haloes of  $10^{13} M_{\odot}$  are dominated by the hot-mode accretion at all of the plotted redshifts, and haloes of  $10^{12} M_{\odot}$  are dominated by hot mode at all but the highest redshifts (see Fig. 6). Unmarked lines show the corresponding predictions of the infall model described above; these correspond to the  $10^{11} M_{\odot}$  model curve (solid line) multiplied by factors of 10 and 100. In these higher-mass haloes, gas must cool before it can accrete on to the central galaxies, so it is not surprising that the pure infall model now overpredicts the galaxy accretion rates. However, the infall model still captures the redshift dependence of these rates remarkably well, especially if one ignores the highest redshifts, where the number of  $10^{13} M_{\odot}$  haloes is small and the  $10^{12} M_{\odot}$  haloes have a significant cold-mode contribution. It is as if cooling just places a constant ‘tax’ on the newly available halo gas, allowing an almost redshift-independent fraction of the gas to cool at a given halo mass. This fraction decreases from  $\sim 0.45$  for  $10^{12} M_{\odot}$  haloes to  $\sim 0.20$  for  $10^{13} M_{\odot}$  haloes, as one might expect given the higher virial temperatures and correspondingly longer cooling times in more massive haloes.

To model the cooling effects in simpler terms, we have followed an analytical prescription along the lines of White & Frenk (1991), assuming spherical haloes with isothermal density and temperature profiles. We suppose that all gas that is able to cool accretes instantaneously on to the central galaxy. The accretion rate is, therefore,  $\dot{M} = 4\pi r_{\text{cool}}^2 \rho_{\text{cool}} dr_{\text{cool}}/dt$ , where  $\rho_{\text{cool}}$  is the gas density at the cool-

ing radius,  $r_{\text{cool}}$ , which is the radius where  $t_{\text{cool}} = t_{\text{H}}$  ( $t_{\text{H}}$  is the Hubble time). Therefore, increasing the cooling radius in time defines the accretion rate. This model predicts accretion rates  $\sim 30$ – $60$  per cent lower than we find for  $10^{12}$  and  $10^{13} M_{\odot}$  haloes, but it reproduces the evolution of these rates fairly well.

At least part of the difference in the magnitude of accretion rates may be a result of our limited numerical resolution. Springel & Hernquist (2002) find that the accretion rates can be overestimated in formulations of SPH such as those that we use here when there are not enough gas particles in the galaxy halo. We have repeated the above analysis for the L11/128 and L5.5/128 simulations (at  $z = 3$  and 4) and find that the accretion rates drop by 40–50 per cent for  $10^{12} M_{\odot}$  haloes. However, each of these simulations has only one halo in this mass range, so this result is only suggestive. Further work using simulations with a higher dynamic range will be needed to fully elucidate the mechanisms that drive the evolution of hot-mode accretion.

With these results in mind, we can build the following interpretation of the accretion rate evolution in Fig. 4, and consequently of the evolution of the cosmic SFR in the simulations. The accretion rate climbs very rapidly starting at  $z \sim 5$  as more galaxies form above the resolution threshold – if we had higher resolution and a lower threshold, the accretion rate at these redshifts would be higher and would evolve more slowly. The number of galaxies in the low-mass regime where cold accretion dominates reaches a maximum at  $z \sim 2$  and declines slowly thereafter. The rapid drop in the global cold accretion rate, starting at  $z \sim 4$ , is driven mainly by the decreasing accretion rate per galaxy shown in Fig. 20, which reflects the increasing infall time-scale in a lower-density universe. The mass threshold for hot accretion is higher, so the hot accretion starts to climb later and peaks at a lower redshift,  $z \sim 2$ . Furthermore, the number density of hot-mode haloes stays roughly constant at  $z < 2$ , and the average mass of these haloes increases with time. (Note that higher-mass haloes always have higher mean accretion rates in both the simulation and the analytic model, even though the ‘cooling tax’ makes the increase slower than  $\dot{M} \propto M$ .) The drop in global hot accretion is, therefore, also a consequence of the fast drop in the accretion rate per galaxy. This drop is slightly slower than for the cold mode owing to an increase in the characteristic mass of hot-mode haloes with time and to a slight increase in their number density.

In broader terms, most accreting galaxies at high redshift are low mass, do not have virial shocks and connect directly to their large-scale environment by filamentary ‘umbilical cords’. At intermediate redshifts, the galaxies experiencing the most accretion are intermediate-mass systems with virial shocks penetrated by cool filaments, accreting in a mix of hot and cold mode. At low redshift, there are many high-mass galaxies with no cold accretion, and many low-mass galaxies reside in high-mass haloes where they experience primarily hot accretion. The filamentary structures that play such a vital role in cold-mode accretion grow in scale as the Universe evolves, particularly around high-density regions. They eventually become too large to feed individual galaxies and instead channel their flows into the hot IGM of groups and clusters. The combination of galaxy mass scales and large-scale structure geometry drives the predicted dependence of the SFR on environment, allowing it to extend beyond the virial radii of large groups and clusters.

One of the most striking features of the galaxy population to emerge from the SDSS is a rapid transition in typical galaxy properties at a stellar mass  $M_{*} \sim 3 \times 10^{10} M_{\odot}$  (Kauffmann et al. 2003; Kannappan 2004). Galaxies below this mass tend to be actively star forming with lower surface densities, high gas fractions and

late-type morphologies, while galaxies above this mass tend to have old stellar populations, high surface density, low gas fraction and early-type morphology. The observed transition mass is remarkably close to that at which we find a transition from cold-mode domination to hot-mode domination, so it is tempting to see the two as connected. It is not clear just how the second transition would bring about the first. However, if a galaxy accretes much of its mass along filamentary structures, this process is bound to influence its angular momentum, perhaps radically modifying the traditional picture of disc formation in which the specific angular momentum distribution of the disc is closely related to that of its parent dark matter halo (Hoyle 1949; Peebles 1969; Fall & Efstathiou 1980; Mo et al. 1998; Bullock et al. 2001a; van den Bosch 2001). In particular, cold accretion might be crucial to disc formation, with hot accretion contributing mainly to spheroid growth. The lower efficiency of hot accretion will also cause high-mass galaxies to have less star formation and older stellar populations, though it is not clear that this effect in itself will produce a transition as strong as the observed one. If, as we speculate in the next section, hot accretion is suppressed in the real Universe by physical processes not represented in our simulations, then the transition would be much sharper. Furthermore, galaxies substantially above the cold-to-hot transition mass would then have to be built by mergers, explaining their predominantly elliptical morphology. A tight connection between cold accretion and disc formation would also help explain the observed morphology–density relation, as the cold accretion fraction depends strongly on environment. For the moment, these remarks are largely speculation, but we hope that future investigations of higher-resolution simulations will deepen our understanding of the cold and hot accretion processes and their connection to galaxy morphologies and stellar populations.

When the baryons within a dark matter halo cool to form the central galaxy in the standard hot-mode picture, the dark matter density near the galaxy increases through adiabatic contraction (Blumenthal et al. 1986). This results in an increase in the circular velocity of the galaxy, which can lead to conflicts with observations. For example, it is difficult for models to simultaneously match the galaxy luminosity function and the zero-point of the Tully–Fisher relation (e.g. van den Bosch, Mo & Yang 2003). However, if the galaxy assembles through cold-mode accretion, adiabatic contraction might not occur or be greatly reduced as the dark matter and baryonic components assemble nearly simultaneously. This might help alleviate some of the tension with observations, especially as most disc galaxies should be cold-mode-dominated, given that on average they have lower masses (e.g. Bell et al. 2003).

The most direct observational tests of cold accretion would come from detecting the cooling radiation associated with gas infall on to galaxies. As emphasized by Fardal et al. (2001), the existence of an important cold accretion mode allows a significant fraction of the gravitational energy acquired by accreting gas to emerge in the Ly $\alpha$  line, producing luminosities that are detectable with large telescopes. The main challenge to this test is separating the contribution of cooling radiation from the contribution of star formation, as galaxies with high accretion rates should also have high star formation rates. Because the Ly $\alpha$  photons from cooling radiation are generally produced at larger galactocentric radii, it should be possible to distinguish the two contributions, but accurate predictions of the angular and frequency distribution of Ly $\alpha$  cooling radiation require radiative transfer calculations that have not yet been applied to three-dimensional simulations. Filamentary gas flows that penetrate close to the galaxy disc and then shock should produce X-ray ‘hotspots’ in the inner regions of some galaxy haloes. Fur-

ther investigation will be required to assess the observability of this phenomenon. High column densities of neutral hydrogen near the disc might absorb much of the X-ray emission and re-radiate it in Ly $\alpha$  (Birnbom & Dekel 2003).

#### 6.4 Accretion and feedback

Although our simulations appear reasonably consistent with the observationally inferred history of cosmic star formation (Fardal et al., in preparation), they overpredict the  $z = 0$  baryonic mass function relative to the observational estimates of, for example, Cole et al. (2001) or Bell et al. (2003). Globally, the predicted fraction of baryons in the form of stars and cold gas exceeds the observationally inferred fraction by a factor of  $\sim 2$ – $3$ . Of course, the integral of the mean cosmic star formation rate must equal the mean stellar mass density (when corrected for the stellar mass loss and recycling of this gas), so the agreement with one and disagreement with the other implies that at least some of the observational estimates of these quantities are themselves in conflict. However, the SFR estimates have substantial systematic uncertainties, while the stellar mass densities appear reasonably secure *if* the assumed stellar initial mass functions (IMFs) are correct, so we think it more likely that the simulations are indeed producing overly massive galaxies. A related problem is that the simulations predict ongoing accretion and star formation in high-mass galaxies, while in the real Universe these systems are predominantly ellipticals exhibiting little or no recent star formation. Similar difficulties with the luminosities and colours of high-mass galaxies appear in semi-analytic models of galaxy formation, unless they are specifically modified to suppress them (see, e.g., Benson et al. 2003).

Simply distinguishing between hot and cold accretion does not, of course, change the simulation predictions. However, the conflicts mentioned above suggest that these simulations are still missing some physical processes that play a significant role in galaxy formation, and these processes might have different effects on hot and cold accretion. One can imagine, for instance, that hot-mode accretion might be more easily suppressed by some forms of feedback because the hot-mode gas is of lower density and more isotropically distributed. In the local Universe, at least, it appears that hot accretion *is* suppressed in groups and clusters, where X-ray emissivities imply short cooling times but X-ray spectra show that the predicted gas at  $T \lesssim 1$  keV is not present (Peterson et al. 2003). The leading hypothesis for explaining this conflict is that the central regions of the intracluster medium are heated by recurrent AGN activity, thermal conduction from the outer regions or both (e.g. Binney & Tabor 1995; Ciotti & Ostriker 2001; Narayan & Medvedev 2001; Ruszkowski & Begelman 2002). The same processes might operate in lower-mass haloes at moderate redshifts. Maller & Bullock (2004) argue that a proper, multiphase treatment of hot halo gas reduces predicted accretion rates by a substantial factor, even without conduction or extra feedback, because the cooling gas forms dense clouds and the remaining gas has lower densities and longer cooling times. This effect is omitted in standard analytic treatments and would be missed by simulations (such as ours) that do not resolve the  $\sim 10^6 M_{\odot}$  scale of clouds formed by thermal instability. Whatever the mechanism, preferential suppression of hot-mode accretion would lead to a sharper cut-off at the high end of the luminosity function, a more rapid decline in the cosmic SFR at  $z \lesssim 1$ , and older stellar populations in massive galaxies. All of these changes would improve the agreement between our SPH simulations and observations, and they would also improve the agreement for most semi-analytic models. Binney (2004) has made similar points, drawing on our preliminary

results (Katz et al. 2003) and the 1D calculations of Binney (1977) and Birnboim & Dekel (2003) for theoretical motivation (see also Dekel & Birnboim 2005).

In our simulations, supernova feedback has little impact on galaxy masses because the supernova energy is usually deposited in a dense medium, where it radiates away before it can drive a galactic wind. Simple models of a multiphase interstellar medium do not change this result (Springel & Hernquist 2003a), but collective effects may allow real galaxies to drive winds more easily, and a number of groups have added ad hoc wind models to simulations (e.g. Theuns et al. 2002; Abadi et al. 2003; Springel & Hernquist 2003a). The interplay of supernova-driven winds with accretion modes might be different from that of conduction or AGN feedback, because once a wind is launched the main challenge is getting it out of the galaxy halo, so that the gas does not simply return and form stars on a short time-scale. In a galaxy fed by filamentary cold accretion, supernova-driven gas might encounter little resistance because there is no surrounding halo medium (see the left-hand panels of Fig. 17). In a galaxy dominated by hot accretion, on the other hand, the disc and bulge are surrounded by a shock-heated gas halo, and a wind may be trapped at small radius. Thus, one can easily imagine that expulsion of cooled gas by supernova feedback, in contrast to the suppression of cooling by AGN feedback or conduction, might operate more efficiently in low-mass galaxies. This might provide a way of reducing the masses of low-mass galaxies and flattening the faint end of the galaxy luminosity function, which would again improve agreement between the simulations and data.

The conventional understanding of supernova feedback also suggests that it will be more effective in low-mass systems because gas is more easily driven out of shallow potential wells (Dekel & Silk 1986). We have focused instead on the role of the surrounding hot gas, which we suspect is even more important, as simulations of the feedback process show that only low-mass galaxies ( $M_{\text{gal}} \lesssim 10^9 M_{\odot}$ ) blow out significant amounts of gas if they are surrounded by conventional hot haloes (Ferrara & Tolstoy 2000). The form of the observed mass–metallicity relation can be understood if supernova-driven winds are efficient below  $M_{\text{gal}} \sim 3 \times 10^{10} M_{\odot}$  and inefficient at higher masses (Tremonti et al. 2004). This transition mass is close to the mass where cold accretion gives way to hot accretion in our simulated galaxies, so it might emerge naturally if trapping by the hot gas halo is the correct explanation for it.

The simulation predictions would also change in interesting ways if we assumed that cold accretion is associated with the conventional stellar IMF (e.g. Miller & Scalo 1979; Kennicutt 1983) but that hot accretion is associated with *either* a bottom-heavy IMF rich in brown dwarfs *or* a top-heavy IMF truncated below  $\sim 2 M_{\odot}$ . In the first case, massive galaxies would have high stellar mass-to-light ratios and therefore lower luminosities. In the second case, the massive galaxies would have lower stellar masses (assuming that much of the recycled gas from evolved stars is driven from the galaxy), and they would have higher UV luminosities during their star-forming phases. Allowing IMF variations introduces a frightening level of freedom in galaxy formation models, but with two physically distinct accretion processes one should at least consider the possibility that the associated star formation is different.

For the moment, these proposals are largely speculation. We are carrying out further investigations to see how the predicted properties of the galaxy population would change if we assume preferential suppression of hot-mode accretion or different stellar IMFs for the two modes. Such adjustments may make distinctive observational predictions that could compensate for the extra freedom they introduce, and their physical underpinnings can be investigated with

higher-resolution simulations focused on these questions. Given the variety of possible assumptions, semi-analytic calculations might be a sensible approach to exploring models that treat cold and hot accretion differently.

## 7 CONCLUSIONS

In SPH simulations of galaxy formation, a substantial fraction of the gas accreted by galaxies is never heated close to the virial temperature of the galaxy potential wells. The importance of this cold accretion mode, relative to the hot accretion mode envisioned in the traditional picture of galaxy formation, depends strongly on galaxy mass. Most galaxies below a baryonic mass  $M_{\text{gal}} \sim 10^{10.3} M_{\odot}$  or dark halo mass  $M_{\text{halo}} \sim 10^{11.4} M_{\odot}$  accrete primarily in the cold mode, while more massive galaxies accrete primarily in the hot mode. As high-mass galaxies are built from lower-mass systems, even galaxies at the top end of the luminosity function today acquired a significant fraction of their mass via cold accretion. Globally, the increasing mass scale of galaxies means that cold accretion dominates at high redshift and hot accretion at low redshift. The ratio of cold to hot accretion is also environment dependent, mostly because higher-mass galaxies are more common in dense environments, and partly because low-mass systems in dense environments have a larger hot accretion fraction than their isolated counterparts. Hot-mode accretion is quasi-spherical, but cold-mode accretion is often directed along filamentary channels, increasing its efficiency.

A number of arguments suggest that these are physical results, not numerical artefacts. A quantitatively important cold mode appears in simulations covering a factor of 512 in mass resolution, though the lowest-resolution simulations do not include a photoionizing UV background and therefore predict a notably different temperature distribution for cold-mode gas. The transition mass of  $M_{\text{gal}} \sim 10^{10.3} M_{\odot}$  is stable in simulations covering a factor of 64 in mass resolution. Cold accretion is seen in other SPH simulations, including one with a substantially different implementation of shock heating. Cold filamentary flows are found in adaptive mesh simulations, though these cannot yet test whether gas gets into galaxies without experiencing strong shock heating. Finally, the transition mass in our simulations agrees (to within a factor of  $\sim 2$ – $3$ ) with that found by Birnboim & Dekel (2003) using entirely independent analytic methods and high-resolution 1D calculations. Despite this litany of tests, we cannot rule out the possibility that cold accretion is an artefact of the finite resolution of shocks in SPH simulations. Confirmation with still higher-resolution simulations and with hydrodynamic methods that directly impose shock jump conditions at velocity discontinuities is therefore desirable. The transition mass separating hot and cold accretion is quantitatively different from the transition mass separating rapid and slow post-shock cooling in semi-analytic models of galaxy formation, at least as calculated by our implementation, which we believe to be the standard one (see Section 6.2 and the Appendix). However, semi-analytic models could be easily revised to incorporate a cold mode of gas accretion calibrated on hydrodynamic simulations such as those analysed here.

Cold accretion could have important implications for the cosmic star formation history and for the correlations of galaxy star formation rates, stellar populations and morphology with environment. If cold and hot accretion are affected differently by stellar or AGN feedback, or if they are associated with different stellar IMFs, then the simulation predictions would change in interesting ways, perhaps resolving conflicts with the observed colours of ellipticals and with the observationally inferred galaxy baryonic mass function.



Our predicted transition mass is close to the observed transition mass at which typical galaxy properties change markedly (Kauffmann et al. 2003), and we have speculated on possible connections between the two. In particular, if AGN feedback, multiphase cloud production, or some other mechanism strongly suppresses hot accretion in the real Universe, then galaxies above the transition mass would have little recent accretion and star formation, and they would have to be built by mergers of lower-mass systems, which would produce spheroidal morphologies. Many questions remain concerning both the underlying physics and the observational implications of cold accretion, but we hope that higher-resolution simulations and comparisons with data will answer these questions over the next few years and solidify our understanding of how galaxies obtain their gas.

## ACKNOWLEDGMENTS

We thank L. Hernquist and V. Springel for allowing us to analyse their Q3 simulation, as discussed in Section 4.5. We thank Y. Birnboim, A. Dekel, A. Kravtsov, A. Maller and H. J. Mo for helpful discussions, C. Murali for providing the merger code used in our analysis, and an anonymous referee for constructive comments. This project was supported by NASA ATP grants NAG5-12038 and NAG5-13308, NASA LTSA grant NAG5-3525, and NSF grants AST-9988146 and AST-0205969.

## REFERENCES

- Abadi M. G., Navarro J. F., Steinmetz M., Eke V. R., 2003, *ApJ*, 591, 499  
 Avila-Reese V., Firmani C., Hernandez X., 1998, *ApJ*, 505, 37  
 Balogh M. L., Pearce F. R., Bower R. G., Kay S. T., 2001, *MNRAS*, 326, 1228  
 Barnes J. E., Hut P., 1986, *Nat*, 324, 446  
 Baugh C. M., Lacey C. G., Frenk C. S., Granato G. L., Silva L., Bressan A., Benson A. J., Cole S., 2005, *MNRAS*, 356, 1191  
 Bell E. F., McIntosh D. H., Katz N., Weinberg M. D., 2003, *ApJS*, 149, 289  
 Bennett C. L. et al., 2003, *ApJS*, 148, 1  
 Benson A. J., Bower R. G., Frenk C. S., White S. D. M., 2000, *MNRAS*, 314, 557  
 Benson A. J., Pearce F. R., Frenk C. S., Baugh C. M., Jenkins A., 2001, *MNRAS*, 320, 261  
 Benson A. J., Bower R. G., Frenk C. S., Lacey C. G., Baugh C. M., Cole S., 2003, *ApJ*, 599, 38  
 Binney J., 1977, *MNRAS*, 215, 483  
 Binney J., 2004, *MNRAS*, 347, 1093  
 Binney J., Tabor G., 1995, *MNRAS*, 276, 663  
 Birnboim Y., Dekel A., 2003, *MNRAS*, 345, 349  
 Blanton M., Cen R., Ostriker J. P., Strauss M. A., Tegmark M., 2000, *ApJ*, 531, 1  
 Blanton M. R. et al., 2003, *ApJ*, 592, 819  
 Blumenthal G. R., Faber S. M., Flores R., Primack J. R., 1986, *ApJ*, 301, 27  
 Bryan G. L., Norman M. L., 1998, *ApJ*, 495, 80  
 Bullock J. S., Dekel A., Kolatt T. S., Kravtsov A., Klypin A. A., Porciani C., Primack J. R., 2001a, *ApJ*, 555, 240  
 Bullock J. S., Kolatt T. S., Sigad Y., Somerville R. S., Kravtsov A. V., Klypin A. A., Primack J. R., Dekel A., 2001b, *MNRAS*, 321, 559  
 Burles S., Tytler D., 1998, *ApJ*, 507, 732  
 Cen R., Ostriker J. P., 1999, *ApJ*, 514, 1  
 Ciotti L., Ostriker J. P., 2001, *ApJ*, 551, 131  
 Cole S., Aragon-Salamanca A., Frenk C. S., Navarro J. F., Zepf S. E., 1994, *MNRAS*, 271, 781  
 Cole S., Lacey C. G., Baugh C. M., Frenk C. S., 2000, *MNRAS*, 319, 168  
 Cole S. et al., 2001, *MNRAS*, 326, 255  
 Colless M. et al., 2001, *MNRAS*, 328, 1039  
 Davé R., Dubinski J., Hernquist L., 1997, *New Astron.*, 2, 227  
 Davé R., Hernquist L., Katz N., Weinberg D. H., 1999, *ApJ*, 511, 521  
 Davis M., Efstathiou G., Frenk C. S., White S. D. M., 1985, *ApJ*, 292, 371  
 de Bernardis P. et al., 2002, *ApJ*, 564, 559  
 Dekel A., Birnboim Y., 2005, *MNRAS*, submitted (astro-ph/0412300)  
 Dekel A., Silk J., 1986, *ApJ*, 303, 39  
 Dressler A., 1980, *ApJ*, 236, 351  
 Efstathiou G., 1992, *MNRAS*, 256, 43p  
 Evrard A. E., Summers F. J., Davis M., 1994, *ApJ*, 422, 11  
 Fall S. M., Efstathiou G., 1980, *MNRAS*, 193, 189  
 Fardal M. A., Katz N., Gardner J. P., Hernquist L., Weinberg D. H., Davé R., 2001, *ApJ*, 562, 605  
 Ferrara A., Tolstoy E., 2000, *MNRAS*, 313, 291  
 Gelb J. M., Bertschinger E., 1994, *ApJ*, 436, 467  
 Gingold R. A., Monaghan J. J., 1977, *MNRAS*, 181, 375  
 Gnedin N., 2000, *ApJ*, 542, 535  
 Gómez P. L. et al., 2003, *ApJ*, 584, 210 (G03)  
 Gunn J. E., Gott J. R., 1972, *ApJ*, 176, 1  
 Haardt F., Madau P., 1996, *ApJ*, 461, 20  
 Haiman Z., Spaans M., Quataert E., 2000, *ApJ*, 537, L5  
 Helly J. C., Cole S., Frenk C. S., Baugh C. M., Benson A., Lacey C., Pearce F. R., 2003, *MNRAS*, 338, 913  
 Hernquist L., 1987, *ApJS*, 64, 715  
 Hernquist L., Katz N., 1989, *ApJS*, 70, 419  
 Hoyle F., 1949, in Burgers J. M., van de Hulst H. C., eds, *Problems of Cosmological Aerodynamics*. International Union Theoretical Applied Mechanical and International Astr. Union, Dayton, p. 195  
 Hubble E. P., 1936, *The Realm of the Nebulae*. Oxford Univ. Press, Oxford, p. 79  
 Hui L., Gnedin N., 1997, *MNRAS*, 292, 27  
 Hutchings R. M., Thomas P. A., 2000, *MNRAS*, 319, 721  
 Kannappan S., 2004, *ApJ*, 611, 89  
 Katz N., Gunn J. E., 1991, *ApJ*, 377, 365  
 Katz N., White S. D. M., 1993, *ApJ*, 412, 455  
 Katz N., Hernquist L., Weinberg D. H., 1992, *ApJ*, 399, L109  
 Katz N., Quinn T., Bertschinger E., Gelb J. M., 1994, *MNRAS*, 270, L71  
 Katz N., Weinberg D. H., Hernquist L., 1996, *ApJS*, 105, 19 (KWH)  
 Katz N., Keres D., Davé R., Weinberg D. H., 2003, in Rosenberg J. L., Putman M. E., eds, *The IGM/Galaxy Connection: the Distribution of Baryons at  $z = 0$* . Kluwer, Dordrecht, p. 185  
 Kauffmann G., White S. D. M., Guiderdoni B., 1993, *MNRAS*, 264, 201  
 Kauffmann G. et al., 2003, *MNRAS*, 341, 54  
 Kauffmann G., White S. D. M., Heckman T. M., Menard B., Brinchmann J., Charlot S., Tremonti C., Brinkmann J., 2004, *MNRAS*, 353, 713  
 Kay S. T., Pearce F. R., Jenkins A., Frenk C. S., White S. D. M., Thomas P. A., Couchman H. M. P., 2000, *MNRAS*, 316, 374  
 Kennicutt R. C., 1983, *ApJ*, 272, 54  
 Kennicutt R. C., 1998, *ApJ*, 498, 541  
 Kitayama T., Suto Y., 1996, *ApJ*, 469, 480  
 Kodama T., Smail I., Nakata F., Okamura S., Bower R. G., 2001, *ApJ*, 562, 9  
 Larson R. B., Tinsley B. M., Caldwell C. N., 1980, *ApJ*, 460, 1  
 Lewis I. et al., 2002, *MNRAS*, 334, 673  
 Lucy L., 1977, *AJ*, 82, 1013  
 Madau P., Ferguson H. C., Dickinson M. E., Giavalisco M., Steidel C. C., Fruchter A., 1996, *MNRAS*, 283, 1388  
 Maller A. H., Bullock J. S., 2004, *MNRAS*, 355, 694  
 Miller G. E., Scalo J. M., 1979, *ApJS*, 41, 513  
 Miralda-Escudé J., Rees M. J., 1994, *MNRAS*, 266, 343  
 Mo H. J., Mao S., White S. D. M., 1998, *MNRAS*, 295, 319  
 Moore B., Katz N., Lake G., Dressler A., Oemler A., 1996, *Nat*, 379, 613  
 Moore B., Lake G., Katz N., 1998, *ApJ*, 495, 139  
 Murali C., Katz N., Hernquist L., Weinberg D. H., Davé R., 2002, *ApJ*, 571, 1 (MKHWD)  
 Nagai D., Kravtsov A. V., 2003, *ApJ*, 587, 514  
 Narayan R., Medvedev M., 2001, *ApJ*, 562, L129  
 Navarro J. F., Frenk C. S., White S. D. M., 1996, *ApJ*, 462, 563  
 Peebles P. J. E., 1969, *ApJ*, 155, 393

- Peterson J. R., Kahn S. M., Paerels F. B. S., Kaastra J. S., Tamura T., Bleeker J. A. M., Ferrigno C., Jernigan J. G., 2003, *ApJ*, 590, 207
- Postman M., Geller M. J., 1984, *ApJ*, 281, 95
- Quinn T., Katz N., Efstathiou G., 1996, *MNRAS*, 278, L49
- Rees M. J., Ostriker J. P., 1977, *MNRAS*, 179, 541
- Ruszkowski M., Begelman M. C., 2002, *ApJ*, 581, 223
- Schechter P., 1976, *ApJ*, 203, 297
- Schmidt M., 1959, *ApJ*, 129, 243
- Seljak U., Zaldarriaga M., 1996, *ApJ*, 469, 437
- Silk J. I., 1977, *ApJ*, 211, 638
- Somerville R. S., Primack J. R., 1999, *MNRAS*, 310, 1087
- Spergel D. N. et al., 2003, *ApJS*, 148, 175
- Springel V., Hernquist L., 2002, *MNRAS*, 333, 649
- Springel V., Hernquist L., 2003a, *MNRAS*, 339, 289
- Springel V., Hernquist L., 2003b, *MNRAS*, 339, 312
- Steidel C. C., Adelberger K. L., Giavalisco M., Dickinson M., Pettini M., 1999, *ApJ*, 519, 1
- Theuns T., Viel M., Kay S., Schaye J., Carswell R. F., Tzanavaris P., 2002, *ApJ*, 578, L5
- Thoul A. A., Weinberg D. H., 1996, *ApJ*, 465, 608
- Tremonti C. et al., 2004, *ApJ*, 613, 898
- van den Bosch F. C., 2001, *MNRAS*, 327, 1334
- van den Bosch F. C., Mo H. J., Yang X., 2003, *MNRAS*, 345, 923
- Weinberg D. H., Hernquist L., Katz N., 1997, *ApJ*, 477, 8
- Weinberg D. H., Davé R., Katz N., Hernquist L., 2004, *ApJ*, 601, 1
- White S. D. M., Rees M. J., 1978, *MNRAS*, 183, 341
- White S. D. M., Frenk C. S., 1991, *ApJ*, 379, 52
- White S. D. M., Efstathiou G. P., Frenk C. S., 1993, *MNRAS*, 262, 1023
- York D. G. et al., 2000, *AJ*, 120, 1579
- Yoshida N., Stoehr F., Springel V., White S. D. M., 2002, *MNRAS*, 335, 762
- Zaldarriaga M., Seljak U., Bertschinger E., 1998, *ApJ*, 494, 491
- Zheng W., Kriss G. A., Telfer R. C., Grimes J. P., Davidsen A. F., 1997, *ApJ*, 475, 469

## APPENDIX: THE RAPID COOLING TRANSITION IN SEMI-ANALYTIC CALCULATIONS

Semi-analytic models of galaxy formation, which trace back to the formalism introduced by White & Frenk (1991), calculate the growth of galaxies fed by the accretion of gas cooling within dark matter haloes. While cooling rates are calculated assuming that the gas initially heats to the halo virial temperature, these calculations do distinguish between a regime of slow cooling, in which accretion from a quasi-hydrostatic gas halo is regulated by the cooling rate, and a regime of rapid cooling, in which no quasi-hydrostatic atmosphere forms and gas accretion is regulated by the infall rate. Given the qualitative resemblance of this criterion to that introduced by Birnboim & Dekel (2003), it is interesting to ask whether the predicted transition between infall- and cooling-dominated accretion is quantitatively similar to the transition between cold and hot accretion found in our simulations. In this Appendix, we describe our calculation of the infall-cooling transition mass, discussed earlier in Section 6.2.

We assume that galaxy haloes initially contain the universal baryonic fraction of gas,  $\Omega_b/\Omega_m$ , with a constant gas temperature equal to  $T_{\text{vir}}$ . We model the initial gas density distribution as an NFW profile (Navarro et al. 1996), and, for simplicity, assume a constant concentration for the NFW profiles, which is typical for  $10^{11} M_\odot$  haloes (Bullock et al. 2001b):  $c = R_{\text{vir}}/r_s = 15/(1+z)$ .  $R_{\text{vir}}$  is the virial radius and  $r_s$  is the scale radius of the NFW halo. For a given halo virial mass,  $M_{\text{vir}}$ ,  $R_{\text{vir}}$  is defined as the radius within which the enclosed density equals  $\Delta_{\text{vir}}$  times the mean mass density of the

universe at that redshift i.e.

$$R_{\text{vir}} = \left( \frac{3}{4\pi} \frac{M_{\text{vir}}}{\Delta_{\text{vir}} \bar{\rho}_m} \right)^{1/3}, \quad (\text{A1})$$

where we use the approximation for  $\Delta_{\text{vir}}$  from Bryan & Norman (1998), which gives similar results to Kitayama & Suto (1996). For comparison we also consider an alternative model where the gas density follows that of a singular isothermal sphere (SIS) with  $T_{\text{gas}} = T_{\text{vir}}$ .

Following White & Frenk (1991), we define the local cooling time of the halo gas,  $t_{\text{cool}}$ , as

$$t_{\text{cool}}(r) = \frac{3}{2} \frac{k_B T \rho_g(r)}{f_g \mu m_p n_H^2(r) \Lambda(T)}, \quad (\text{A2})$$

where  $k_B$  is the Boltzmann constant,  $\mu$  is the mean ‘molecular’ weight, which we assume to be that of a fully ionized gas,  $f_g$  is the fraction of halo gas available for cooling,  $m_p$  is the proton mass,  $n_H$  is the hydrogen density,  $\rho_g$  is the total gas density and  $\Lambda(T)$  is the cooling function. Like in the simulation, we assume that the gas is primordial with a hydrogen mass fraction of 0.76. The cooling time determines the cooling radius  $r_{\text{cool}}$  at which gas can radiate its thermal energy in a specified amount of time. White & Frenk (1991) define the cooling radius by setting  $t_{\text{cool}}(r_{\text{cool}})$  equal to the Hubble time  $t(z)$ , the age of the Universe at redshift  $z$ . However, different groups use different characteristic times in their semi-analytic calculations. Therefore, to cover a range of possibilities we compare the cooling time to three time-scales: the Hubble time  $t(z)$ , the dynamical time defined as

$$t_{\text{dyn}} = \sqrt{\frac{3\pi}{16G\bar{\rho}(z)}}, \quad (\text{A3})$$

where  $\bar{\rho}$  is the average enclosed density and the free-fall time, which is  $t_{\text{ff}} = t_{\text{dyn}}/\sqrt{2}$ . Therefore, the cooling radius is defined as the radius where  $t_{\text{cool}}(r_{\text{cool}}) = t(z)$ ,  $t_{\text{dyn}}(z)$  or  $t_{\text{ff}}(z)$ . In White & Frenk (1991), infall-dominated accretion takes place when  $r_{\text{cool}} > R_{\text{vir}}$ , and cooling-dominated accretion takes place when  $r_{\text{cool}} < R_{\text{vir}}$ . The transition halo mass between the two regimes is thus the halo mass for which  $r_{\text{cool}} = R_{\text{vir}}$ .

To fairly compare this mass with the transition mass between cold- and hot-mode accretion in our simulations, we use the same cosmology (see Section 2.1) and the same cooling function (see KWH96) as in our simulations, neglecting only inverse Compton cooling. As some gas has already transformed into stars, the fraction of the gas available for cooling,  $f_g$ , is less than one and decreases with redshift. We approximate  $f_g = 1 - 0.28/(1+z)$ , which roughly matches the global fraction of the baryons in the simulation that are not in stars or cold galactic gas at a given redshift.

The UV background affects gas cooling in our simulations after  $z = 6$ , so to make a fair comparison it is necessary to include it in our calculation. As mentioned in Section 4.4, for typical densities at the virial radius, the UV background can significantly alter the hydrogen and helium line cooling peaks in the cooling function, making the cooling times at the virial radius significantly longer.

In Fig. A1, solid lines show the transition mass between infall- and cooling-dominated accretion for an NFW density profile in the presence of the UV background. Squares correspond to a definition of  $r_{\text{cool}}$  with  $t_{\text{cool}} = t(z)$ , triangles to  $t_{\text{cool}} = t_{\text{dyn}}(z)$  and the star to  $t_{\text{cool}} = t_{\text{ff}}(z)$ . For direct comparison we plot the mass where the transition between cold and hot mode occurs in our simulations as the dot-dashed line with circles. At  $z \geq 1$  the transition mass in the simulation is a factor of 2–4 higher than the highest of the semi-analytic transition masses, defined for  $t_{\text{cool}}(R_{\text{vir}}) = t(z)$ . At

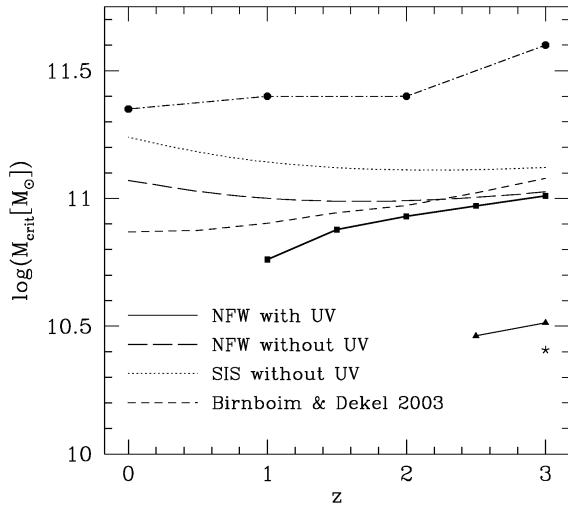


**Figure A1.** Transition halo mass between infall- and cooling-dominated accretion, calculated in a manner similar to that of White & Frenk (1991). Squares, triangles and the star at  $z = 3$  assume an NFW gas density profile with a UV background and a cooling radius definition  $t_{\text{cool}}(r_{\text{cool}}) = t(z)$ ,  $t_{\text{dyn}}(z)$  and  $t_{\text{ff}}(z)$ , respectively. With a UV background, all haloes are cooling dominated below  $z = 1$ , 2.5 or 3, respectively, for these three cases. The dashed line assumes an NFW profile but no UV background, and the dotted line assumes an SIS profile with no UV background, both for  $t_{\text{cool}}(r_{\text{cool}}) = t(z)$ . Filled circles show the transition halo mass at which we find equal amounts of cold and hot accretion in the L22/128 simulation, which includes a UV background. For comparison we also show results from the model of Birnbom & Dekel (2003) (see the text).

$z < 1$ , there is no halo mass for which  $t_{\text{cool}}(R_{\text{vir}}) \leq t(z)$ , so the semi-analytic calculation predicts no infall-dominated haloes at all. If we define the transition with respect to  $t_{\text{dyn}}$  or  $t_{\text{ff}}$ , the semi-analytic transition mass drops by another factor of 3–4 at high redshift, and infall-dominated haloes disappear after  $z = 2.5$  ( $t_{\text{dyn}}$ ) or  $z = 3$  ( $t_{\text{ff}}$ ).

The long-dashed curve in Fig. A1 shows the effect of omitting the UV background, which increases cooling rates and therefore increases the transition mass. With no UV background, there are infall-dominated haloes all the way to  $z = 0$ , though the transition mass is still lower than the cold-hot transition mass in our simulations with a UV background. Furthermore, as discussed in Section 4.4, the increased cooling in the absence of a UV background leads to a

substantially higher transition mass in our simulations themselves. As our simulations without a UV background are lower resolution or run only to  $z = 3$ , we do not have a very accurate measurement of this increase, but it appears to be at least a factor of 4. The dotted curve in Fig. A1 shows the effect of assuming an SIS gas profile instead of an NFW profile, again with no UV background. As an SIS profile has a higher gas density at the virial radius than an NFW profile, the transition mass increases. However, while gas and dark matter profiles inside haloes will generally be different from some degree, the NFW assumption seems likely to be more realistic near the virial radius. For comparison we also plot the model of Birnbom & Dekel (2003, zero metallicity line from the upper panel of their fig. 11), which is motivated by their 1D simulations. Their cosmology is different from ours, but the baryonic mass fraction, one of the main factors determining the transition mass, is similar. Birnbom & Dekel (2003) do not include a UV background in their calculations, and their model agrees fairly well with the ‘NFW without UV’ line in Fig. A1, though the redshift dependence is somewhat different. Dekel & Birnbom (2005) discuss the dependence of the derived transition mass on details of the calculational assumptions, gas metallicity and cosmological parameters.

We conclude that the conventional definition of the transition between infall- and cooling-dominated accretion does not correspond quantitatively to the transition between cold- and hot-mode accretion found in our simulations, if one makes the same physical assumptions in the semi-analytic calculation. However, it may be possible to alter the semi-analytic calculation, for example by defining the transition at some fraction of the virial radius instead of at  $R_{\text{vir}}$  itself, so that the correspondence is better. It would be particularly interesting to see whether a definition of transition mass calibrated to match hydrodynamic simulations for one set of cosmological parameters and cooling rates then reproduces the results of simulations that assume different parameters or different cooling rates (e.g. because of different metallicity or a change of the UV background). A successful analytic model of this sort would provide physical insight into the distinction between cold and hot accretion, and it would be a useful practical tool for investigating the effects of parameter variations.

This paper has been typeset from a  $\text{\TeX}/\text{\LaTeX}$  file prepared by the author.